

RAM

● ROBOTICS
AND
MECHATRONICS

QUALITATIVE FLOW SENSING WITH 3D-PRINTED SENSORS FOR APPLICATION IN A ROBOTIC BIRD

R. (Roosmarijn) Meijers

BSC ASSIGNMENT

Committee:

prof. dr. ir. G.J.M. Krijnen
ir. A.P. Dijkshoorn
dr. ir. T.H.J. Vaneker

August, 2022

028RaM2022
Robotics and Mechatronics
EEMCS
University of Twente
P.O. Box 217
7500 AE Enschede
The Netherlands

Abstract

For drones to be aware of their surrounding and to be able to respond to complex environments, flow sensors can be useful. Numerous quantitative air flow sensors already exist, but qualitative air flow sensors are less common. Especially sensors equipped to measure quickly changing flows, such as the airflow around flapping flight based drones. The aim of this bachelor assignment is to design a sensor that is suitable for drones that use flapping flight and measures the quality of an airflow, in particular the presence of flow reversal. The concept of a strain gauge is used to measure the bending of the sensor. The main challenge is to design a strain gauge with a significant change in resistance when the sensor is bent, while not making the sensor too stiff. The latter is because the sensor needs to sense the flow and so the wind needs to bend the sensor and not be significantly affected. The first step was to find the connection between the aeroelastic behaviour and mechanical properties of the sensor. This was done by testing sensors with different dimensions in a wind tunnel and observing their behaviour. Using these results ten sensors were designed and tested in a wind tunnel. The product of this research are sensors of which the standard deviation of the resistance is dependent on the direction of an airflow. Because of this research flow sensors for quickly changing flows can be made and optimized. In particular, the Robotics and Mechatronics work group of the University of Twente can use this flow sensor to study the airflow around the wings of the Robird better.

Preface

For the past three months I have been working on my bachelor thesis and finishing up my bachelor in Electrical Engineering at the university of Twente. I went out of my comfort zone and chose an assignment where Mechanical Engineering and Aerodynamics also played a big role. Besides my assignment I was also preparing for my board year for E.T.S.V. Scintilla which took more time than I expected. I am grateful that I was granted enough time to finish my assignment and I am satisfied with the result.

I would like to thank the following people for their contributions:

My supervisors Alexander Dijkshoorn and Gijs Krijnen for their support, feedback and ideas that helped improve the quality of my research.

Patrick Bos for his help on explaining the blockage effect in wind tunnels.

All of the members of the biweekly NIFTy meetings for their helpful insights.

Tom Vaneker for being the external member of my bachelor assignment committee.

Remco Sanders for lending his high speed camera to me.

And last but not least, my friends and family for supporting me.

Roosmarijn Meijers
Enschede, 24 July 2022

Contents

1	Introduction	1
2	Theoretical analysis	3
2.1	Strain gauge	3
2.2	Materials	3
2.3	Mechanical properties	4
2.4	Aerodynamics	7
3	Design	11
3.1	Design of the sensors	11
3.2	Fabrication	13
3.3	Conclusion	15
4	Method	16
4.1	Test set-up	16
4.2	Measurement methodology	19
4.3	Conclusion	19
5	Results	20
5.1	Cauchy ratio as function of behaviour in stall	20
5.2	Strain gauge	21
5.3	Conclusion	29
6	Discussion	31
6.1	Mechanical properties of the sensor	31
6.2	Method	31
6.3	Results	31
6.4	Conclusion	33
7	Conclusion	34
A	Formulas	35
B	Results	36
B.1	Resistance change of sensors with strain gauges over time	36
B.2	Resistance means of sensors with strain gauges	38
B.3	Frequency spectrum of sensors with strain gauges	40
B.4	Resistance standard deviation of sensors with strain gauges	42
	Nomenclature	44

Bibliography

46

1 Introduction

For drones to be aware of their surrounding and to be able to respond to complex environments, flow sensors can be useful [1]. Numerous quantitative air flow sensors, which can determine the velocity of an air flow, already exist [2]. But qualitative air flow sensors, which measure the direction of an air flow, are less common. Especially sensors equipped to measure quickly changing flows, such as the air flow around flapping flight based drones, are less common.

In 2021 van den Berg researched to what extent it is possible to use the principle of a piezoresistive strain gauge in a 3D-printed sensor to measure the presence of stall over an airfoil in a qualitative way [3]. This subject was mostly inspired by the work of Bot et al. [4] in which a strain gauge based flow sensor for hydrofoils is tested, a so-called hydro E-telltale. Van den Berg experimented with different lengths of the strain gauges and different angles of attack (AOA). The conclusion of his research was that the effect of the AOA on the flow around the airfoil could be visually observed, but could not be measured through the output of the sensor because the fluctuations of the tuft could not be seen in the resistance data. [3]. The results of this visual observation, which was done by observing the movement of the sensor with a high speed camera, can be seen in table 1.1. The Cauchy number used in this table is related to the dynamic pressure and free stream velocity of the air, the elasticity modulus and the slenderness ratio of the sensor [5], this quantity is explained further in section 2.4. The designed sensor can be seen in figure 1.1.

Length (mm)	20	30	40	50	75
Cauchy number	424.35	1432.2	3394.8	6630.5	22378
No movement	$\alpha < 12.5$	$\alpha < 12$	$\alpha < 12$	$\alpha < 12$	$\alpha < 12$
1D flapping	$\alpha \geq 12.5$	$\alpha \geq 12$	$12 \leq \alpha < 13$	$\alpha = 12$	-
Swishing	-	-	$13 \leq \alpha < 14$	$12 < \alpha < 13$	$12 \leq \alpha < 13.5$
Reversed	-	-	$\alpha \geq 14$	$\alpha \geq 13$	$\alpha \geq 13.5$

Table 1.1: Aeroelastic behaviour of the sensors tested at velocity $U_\infty = 10 \text{ ms}^{-1}$ [3]

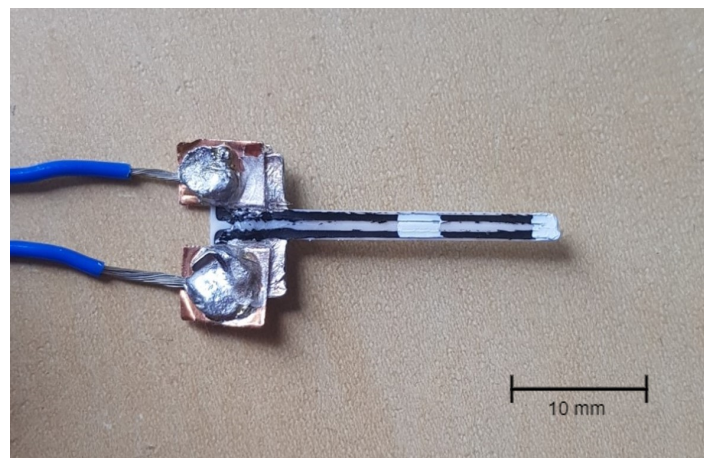


Figure 1.1: The sensor designed by van den Berg [3]

The hydro E-telltale [4] on the other hand did have a clear output for different AOAs, this can be seen in figure 1.2. The output of the sensor has small fluctuations at small AOAs, where

the flow is attached. When the AOA increases, the output fluctuates more as the flow becomes more turbulent. The mean of the output also increases with the angle of attack.

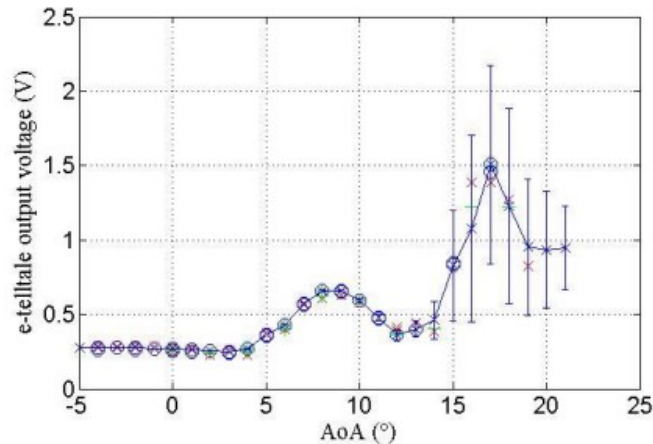


Figure 1.2: The E-telltale output voltage for different angles of attack, error bars show the standard deviation of fluctuations in time series measurements [4]

The aim of this bachelor assignment is to design a sensor that is suitable for aerial drones that use flapping flight, such as the Robird [6]. This flow sensor will be used to measure the quality of an air flow, in particular flow reversal. The following research question is central in this paper:

“How can the presence of flow reversal at the suction side of an airfoil be measured using a 3D-printed flow sensor?”

The main challenge of this assignment is to design a strain gauge with a significant change in resistance when the sensor is bent, while not making the sensor too stiff. The latter is because the sensor needs to sense the flow and so the wind needs to bend the sensor and not be significantly affected by it. To answer the research question, the following sub questions are answered:

- How do mechanical properties of the materials and the structure influence the performance of the strain gauge theoretically?
- How is the Cauchy ratio related to the aeroelastic behaviour of the sensor?
- How can the aeroelastic behaviour of the sensor be determined using the output of the strain gauge?

Van den Berg’s research is used as a basis. The sensor is designed using the concept of a strain gauge, fabricated using 3D-printing and tested in a wind tunnel.

In the second chapter of this report, a theoretical analysis of the strain gauge is done and the first sub question is answered. In the next chapter the design choices for the sensors and the fabrication process are explained. After that the method for testing the sensors is described. In the fifth chapter the results of these test are presented. The discussion, discusses the results and gives recommendations for follow up researches. This reports and with the summary and conclusion of this research are presented and the research question is answered.

2 Theoretical analysis

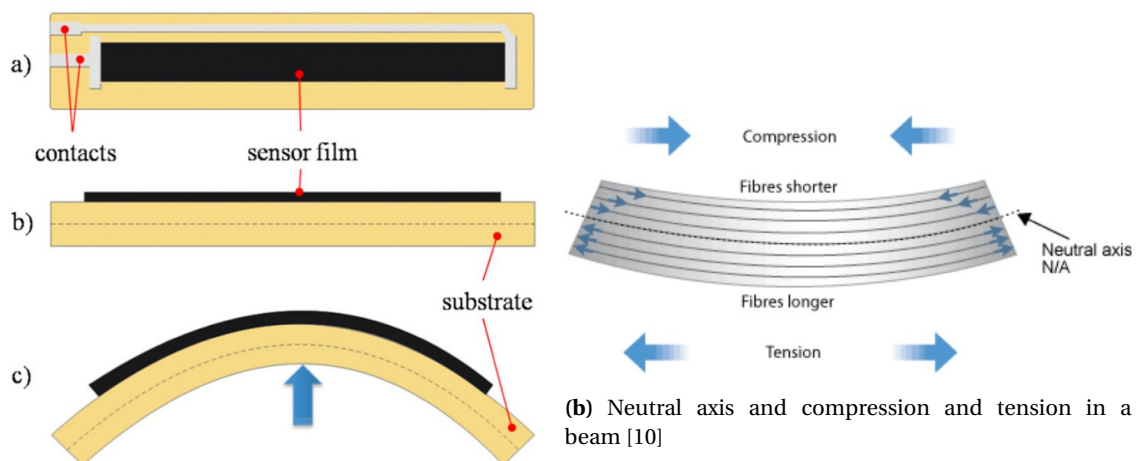
To design a sensor that can measure the change of an airflow and to predict what will be measured, a theoretical analysis is done. This research continues on the research of van den Berg and so the sensor will also be made using the concept of a strain gauge [3]. In this chapter the concept of a strain gauge is described first. Then some materials and their properties are introduced. After this, relevant mechanical properties of the sensor are evaluated. Lastly the aerodynamic and aeroelastic behaviour of the sensor and the airfoil are introduced.

2.1 Strain gauge

A strain gauge works using the concept of resistance change in deformed materials. The equation of the resistance of a sample is shown below.

$$R = \rho \frac{l}{A} \quad [7] \quad (2.1)$$

When the conductive material is compressed, then the length decreases and the cross-section area increases. This results in a lower resistance. With the same principle the resistance increases when tension is applied to the material. However, for semiconducting materials the change in resistivity is the primary cause for the change in resistance. When tension is applied, then the resistivity decreases and thus the resistance decreases as well. Strain gauges that are mostly dependent on this effect are called piezoresistive strain gauges. [8] So for a strain gauge to work, the conductive material needs to be compressed or stretched. All the forces in a structure in rest sum up to zero, so a base is used to ensure that the net force in the strain gauge is not zero. As this force is measured in the form of resistance change the current should only flow through the gauge and thus the base is made from a non-conductive material.



(a) A strain gauge with (a) top view, (b) lateral view and (c) an applied force with lateral view [9]

Figure 2.1: The concept of a strain gauge

2.2 Materials

Fused deposition modeling (FDM) is a manufacturing method based on 3D printing using polymer-based fillaments [11]. FDM is the most popular 3D printing method, it can be used to make detailed structures and it is also more accessible for non-commercial use than other 3D printing methods. The flow sensor that is designed in this report will also be made using FDM.

The flow sensor consists of two materials. Both materials need to be flexible, as they need to be deformed by the airflow. The base is made from the non-conductive thermoplastic polyurethane, short TPU, Ninjaflex [12] and the strain gauge is made from the conductive TPU PI-ETPU [13]. These materials were chosen for their flexibility and availability in the lab.

The PI-ETPU filament consists of a non-conductive flexible thermoplastic doped with conductive carbon black particles [13]. In figure 2.2, the distribution of some carbon black particles in the thermoplastic host material can be seen.

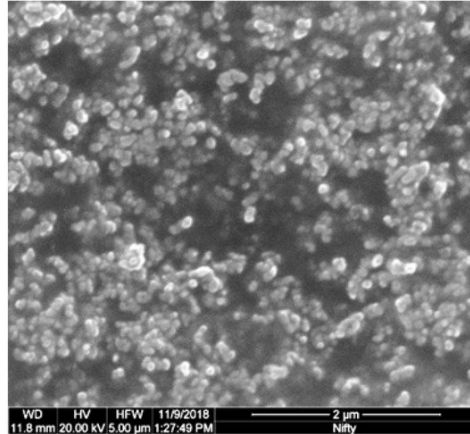


Figure 2.2: Scan of PI-ETPU 85-700+ made with an electron microscope [14]

The distribution of particles in PI-ETPU can change over time, this changes the network formed by the carbon black particles and can be measured as a change of resistance in samples. The resistance change is mostly present when the sample is non-annealed during the first day after printing. In the best case the resistance becomes stable after two days. [15] Annealing is a heat treatment process, that can be used to relieve stress from materials. [16]

Ninjaflex has a Young's modulus of approximately 12 MPa [17] and PI-ETPU has a Young's modulus of ranging from 16 MPa to 18 MPa dependent on the frequency [17]. The loading frequency is unknown, so the worst case scenario, where the difference in Young's modulus is biggest, is used which is 18 MPa.

2.3 Mechanical properties

For the strain gauge to work the conductive part has to be compressed or stretched. In section 2.1 it was shown that for this to happen, a base is needed. The base and the strain gauge have a different Young's moduli which makes the strain gauge material more stiff than the base material. In this section the impact of this difference is evaluated. This is done by introducing the neutral axis and the second moment of inertia. Another mechanical property which is explained in this section is the slenderness ratio, which is needed for the calculation of the Cauchy number (this Cauchy number is elaborated more in section 2.4 Aeroelasticity).

2.3.1 Neutral axis

The neutral axis of a body is the axis where neither compression nor tension occurs when a force is applied on the body [18]. When working with composite structures, the difference in Young's moduli has to be accounted for. This is done by assuming both materials have the same Young's modulus and adjusting the size of the cross-section to compensate for the difference with the actual Young's modulus. The neutral axis of a composite body is calculated using the area of the different layers, their separate neutral axes and the difference in Young's moduli, see

equation 2.2.

$$\bar{y} = \frac{A_1 \bar{y}_1 + nA_2 \bar{y}_2}{A_1 + nA_2} \text{ with } n = \frac{E_2}{E_1} \quad [19] \quad (2.2)$$

When a force is applied to a structure, all the material at one side of the neutral axis will be compressed and the material on the other side of the neutral axis will be stretched. In rest, the force above the neutral axis will be equal and opposed to the force below the neutral axis. The net force will thus be zero. [18] The neutral axis is important to the strain gauge as it measures these forces, but since the forces are opposite on either side of the neutral axis they counter each other when both are being measured. So it is preferred to have the strain gauge entirely on one side of the neutral axis. This gives that the neutral axis is preferred to be located in the base.

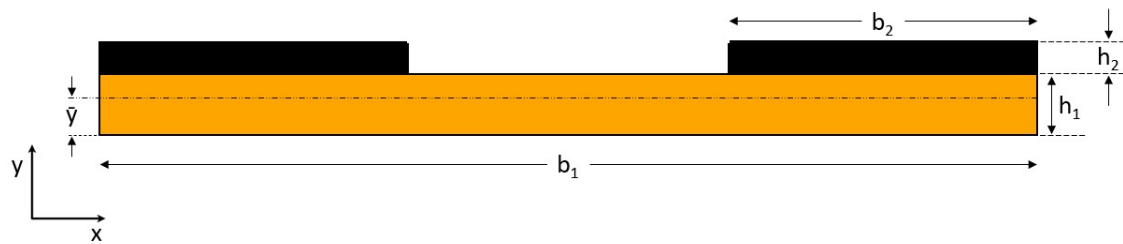


Figure 2.3: Front view of the sensor, with \bar{y} the neutral axis, the base of Ninjaflex in orange and the strain gauge of PI-ETPU in black

The front view of the schematic of the sensor can be seen in figure 2.3. For rectangular shapes the neutral axis is located in the middle, so each layer has its neutral axis also in the middle. Ninjaflex has a Young's modulus of approximately 12 MPa [17] and PI-ETPU has a Young's modulus of approximately 18 MPa [17], so $n \approx \frac{3}{2}$.

In order to have more strain in the strain gauge and thus a bigger change in resistance, the neutral axis can be made lower. To do this the gap between the two lines of the strain gauge could be extended into the base, see figure 2.4. This will only lower the neutral axis if it was already below half of the sensor, then there is more material removed above the neutral axis than below.

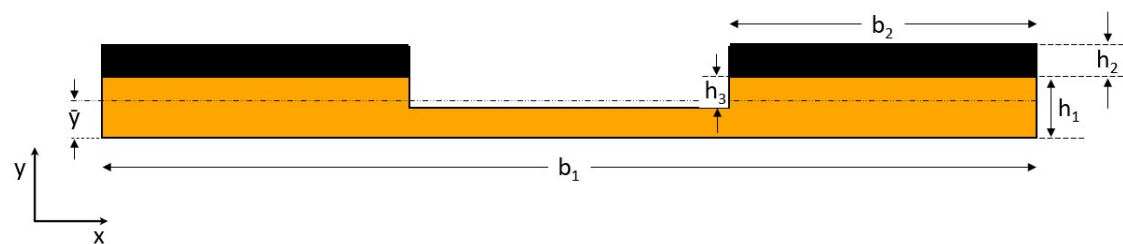


Figure 2.4: Front view of the sensor with extra gap, with \bar{y} is the neutral axis, the base of Ninjaflex in orange and the strain gauge of PI-ETPU in black

2.3.2 Second moment of area

The second moment of area is a measure of how resistant a structure's geometry is against bending in a certain direction. A higher second moment of area means that a larger external moment has to be applied for the structure to bend. The second moment of area is thus dependent on orientation. The second moment of area is calculated by summing the area of a

cross-section multiplied by the square of the distance between this area and the neutral axis. Since the distance is not constant, a more elegant way to calculate the second moment of area is by an integral over the cross section, see equation 2.3. A big area, far away from the neutral axis, results in a higher second moment of area, and a small area close to the neutral axis results in a lower second moment of area. [20]

$$I_i = \int_{A_i} r^2 dA_i \quad (2.3)$$

The second moment of area becomes more complicated for composite beams. The same technique as in section 2.3.1 can be used where the size of the cross-section is adjusted. For the calculation of the second moment of area this is done using equation 2.4. With $n = \frac{E_2}{E_1} = \frac{3}{2}$, see section 2.3.1.

$$I_a = I_1 + \sum n_i I_i \quad [21] \quad (2.4)$$

The second moment of area is important to the sensor because the sensor is based on the air flow (easily) bending the thin beams. So the sensor should bend when a small force is applied and thus a small second moment of area is preferred.

2.3.3 Slenderness ratio

The slenderness ratio is a ratio between the length of a beam and the lesser radius of gyration of both directions. It is mostly used to express how prone a material is to buckling, for a higher slenderness ratio failure by buckling is more common. [22] Buckling is a lateral deflection which occurs when a critical force is applied to the length of a structure. [23]

The forces on the sensor are caused by the airflow. When the sensor does not follow the direction of the airflow, then the air will collide with the sides of the sensor. This results in a force perpendicular to the sensor and a force along the sensor, see figure 2.5. It can be seen that there is some tension on the sensor caused by the airflow. The flexibility of the material makes the sensor less prone to buckling than rigid materials, but buckling could occur over time. In this research the slenderness ratio is mainly used for compensating mechanical properties of very slender structures.

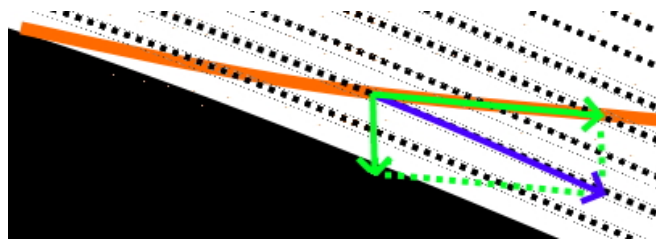


Figure 2.5: Forces on the sensor, sensor in orange, airfoil in black, dotted black line indicates the airflow, resulting force on the sensor in blue and its components in green

The least radius of gyration is used to calculate the slenderness ratio. The radius of gyration is calculated using equation 2.5. For the least radius of gyration, the least second moment of area, i.e. for the various bending directions, is used. The sensor will be much wider than high, so $b \gg h$. So the smallest second moment of area is thus when force is applied perpendicular to the x -direction.

$$r_a = \sqrt{\frac{I_a}{A}} \quad [24] \quad (2.5)$$

The definition of the slenderness ratio is shown below:

$$S = \frac{l}{r_x} \quad [22] \quad (2.6)$$

2.4 Aerodynamics

When designing a flow sensor, not only the sensor itself needs to be understood but the air flow that is measured as well. In this section the lift and stall are explained to gain more insight in what the sensor needs to measure. The Cauchy ratio is also introduced as it gives more insight as to how the sensor influences the airflow and vice versa.

2.4.1 Lift and drag

Lift is an upward force created by a pressure difference between the suction (top) and pressure (bottom) side of an airfoil. When air flows around the airfoil, the air on the suction side of the airfoil has to travel a larger distance than the air on the pressure side. To line up at the trailing edge of the airfoil the air on the suction side has a higher velocity than the air on the pressure side. According to the Bernoulli equations, a flow with a higher velocity has a lower pressure. So the difference in velocity results in a difference in pressure which causes the lifting force. Drag is a force in the opposite direction of the velocity and is caused by the wake of the airfoil. [25]

In wind tunnels the normal (N) and axial (A) forces on a structure can be measured. Together with the angle of attack the lift and force can be calculated, see equation 2.7 and 2.8. The different forces on an airfoil can be seen in 2.6, here R is the resultant aerodynamic force.

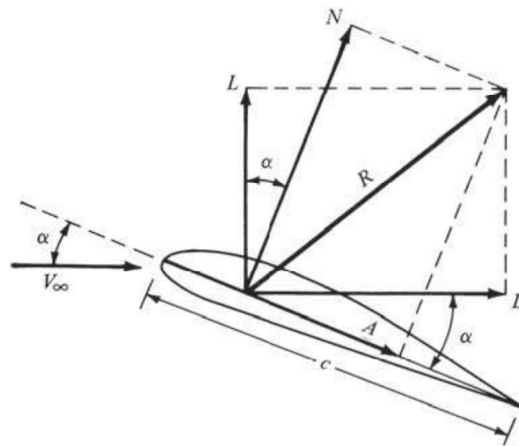


Figure 2.6: Forces on an airfoil [25]

$$L = N \cos \alpha - A \sin \alpha \quad [25] \quad (2.7)$$

$$D = N \sin \alpha + A \cos \alpha \quad [25] \quad (2.8)$$

2.4.2 Stall

In aerodynamics various types of flows are distinguished, two of which are laminar and turbulent flow. Laminar flow is present when the streamlines are smooth, in case of an airfoil this is a flow that sticks to the surface and follows its shape. Turbulent flow occurs when the streamlines separate in irregular and random flow. When a turbulent flow occurs on an airfoil, then this is referred to as stall. [25]

When stall occurs, then a drop in lift force can be observed. Lift is dependent on the geometry of the airfoil and the dynamic pressure of the air. The lift coefficient c_L is used to compare situations where these variables differ. The lift coefficient is calculated by dividing the lift over the dynamic pressure and the wing area, see equation 2.9. The dynamic pressure is dependent

on the density of the air and the relative velocity of the airfoil squared. Stall happens when the lift coefficient drops, an example of this can be seen in figure 2.7. [25]

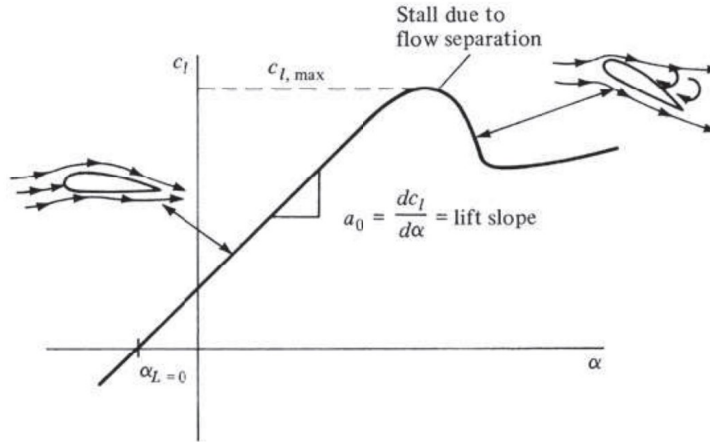


Figure 2.7: Lift coefficient against angle of attack, stall occurs after $c_{L,max}$ has been reached [25]

$$c_L = \frac{L}{qS} \quad \text{with } q = \frac{\rho_f U_\infty^2}{2} \quad [25] \quad (2.9)$$

$$c_D = \frac{D}{qS} \quad \text{with } q = \frac{\rho_f U_\infty^2}{2} \quad [25](2.10)$$

In this research the presence of flow reversal is measured, this flow reversal occurs in stall. To verify that the measurements are done in stall, the lift coefficient is plotted against the angle of attack. When a drop in lift coefficient is seen, then flow reversal can be observed.

2.4.3 Blockage effect

The sensor is investigated in a wind tunnel while equation 2.9 is based on freestream conditions [25]. But in a wind tunnel this is not the case. The walls of the wind tunnel block the airflow. This causes more air to collide with the airfoil than in a freestream and result in an increasing lift, even when stall occurs. This is called the blockage effect and it occurs when the airfoil takes up more than 5% of the cross section area of the wind tunnel. [26]

There are different, complicated, theories on how to correction for this blockage effect. This research only looks at the lift coefficient to verify when stall occurs, so there is chosen to not correct for the blockage effect, but to compare the lift and the drag coefficients, see equation 2.10, and derive from that when stall occurs.

2.4.4 Cauchy number

Aeroelasticity is the study of the interaction between aerodynamics, inertia and elastic forces [27]. In other words, the study of how an elastically deformable object can influence and is influenced by an airflow. The Cauchy number is a dimensionless number which represents the ratio of the inertial force effect of a fluid and the bulk modulus of elasticity of the solid, see equation 2.11. The inertial force effect is calculated by multiplying the density of the air and the squared relative velocity of the airfoil. The higher the Cauchy number, the more the solid structure deforms under the pressure in the fluid. [5]

$$Ca = \frac{\rho_f \cdot U_\infty^2}{K} \quad [28](2.11)$$

The bulk modulus is a measure of the resistance of a material against applied stress in multiple directions [29]. The bulk modulus can be calculated from the Young's modulus and the Poisson's ratio of a material, see equation 2.12.

$$K = \frac{E}{3(1 - 2\nu)} \quad [29](2.12)$$

Poisson's ratio is a measure of how the transverse strain and longitudinal strain are related [30]. Elleuch et al. [31] assumed in his research that TPU has a Poisson's ratio of 0.45, but Qi and Boyce [32] concluded that at room temperature TPU is in a rubbery state and thus has a Poisson's ratio ranges from 0.48 to 0.50. So in this research a Poisson's ratio of 0.48 is assumed for TPU. This gives that the bulk modulus of Ninjaflex is 100 MPa.

De Langre [33] concluded in his research that very slender structures, such as plants have a low Cauchy number, which indicates no deformations, but did have strong deformations. So for slender structures the Cauchy number needs to be corrected with a slenderness factor of S^3 . The results of this correction is a ratio different from the Cauchy number, so from now on this will be referred to as the Cauchy ratio. The Cauchy ratio is calculated using equation 2.13.

$$Ca = \frac{\rho_f \cdot U_\infty^2 \cdot S^3}{K} \quad [33](2.13)$$

Van den Berg [3] used in his research the Young's modulus instead of the bulk modulus to calculate the Cauchy ratio, which is a factor 0.12 smaller. So for the rest of this research when there is referred to the Cauchy ratio of van den Berg's sensors, the values have been corrected with this factor 0.12.

The Cauchy ratio could also be calculated based on a cross section perpendicular to the one in figure 2.3. But this Cauchy ratio would be mostly dependent on torsion and since the sensor is very wide compared to its height, this Cauchy ratio would be much lower. So this effect is less significant than the effect caused by deformations along the length of the sensor. So it is decided to mainly focus on the Cauchy ratio caused by deformations along the length of the sensor.

2.4.5 Conclusion

This chapter starts with explaining the workings of a strain gauge and introduces the materials of which the strain gauge based sensor is made.

In the introduction the sub question "How do mechanical properties of the materials and the structure influence the performance of the strain gauge theoretically?" was introduced. In section 2.3.1 it was concluded that a neutral axis as far away from the strain gauge is preferred for optimal results and two design cross sections were introduced. In section 2.3.2 it was concluded that a lower second moment of area also gives better results. For both the neutral axis and the second moment of area, the difference in Young's moduli of the materials plays a role. These are some of the main mechanical properties of the materials and the structure that influence the performance of the strain gauge, with further analysis the working of the strain gauge could be understood better to design a more optimal sensor.

Furthermore the slenderness ratio was introduced, as it is used to compensate the Cauchy number. In section 2.4, lift and stall were explained and how to compensate for the blockage effect in the wind tunnel.

A higher Cauchy ratio is preferred in the design of the sensor as the sensor deforms more under the pressure in the air. But a higher Cauchy ratio would also mean a thinner and longer sensor. The height of the sensor is limited by the functionality of the sensor, in section 2.3.1 and 2.3.2 it is seen that a thicker sensor gives a better strain gauge output. The length of the sensor is

limited by the airfoil the sensor will be placed on. Stall originates from the trailing edge and expands to the leading edge. A very long sensor will not be entirely in stall and will sense less. So a consideration in dimensions of the sensor should be made.

3 Design

Using the theory from the previous chapter, the design of the sensor is made. This sensor is fabricated using a 3D printer and after fabrication the performance of the sensor is tested. This chapter first describes the design choices of the sensor. Then the fabrication process is described. Lastly the test set-up in which the performance of the sensor is measured is described.

3.1 Design of the sensors

To get an idea of what dimensions to use for the sensor, first some tests with sensors without a strain gauge will be performed. This is to gain an insight as to which dimensions and Cauchy ratios show promising results. The strain gauge is left out for these tests as printing with multiple materials takes more time than printing with only one.

3.1.1 Cauchy ratio as function of behaviour

The first batch of sensors that will be tested are made entirely from Ninjaflex. For simplicity in calculating the Cauchy ratio, the sensor is a rectangular block. Combining the equations 2.5, 2.6, 2.13 and the second moment of inertia of a rectangular block, see equation 3.1, gives equation 3.2.

$$I_x = \frac{bh^3}{12} \quad [20] \quad (3.1)$$

$$Ca = \frac{\rho_f \cdot U_\infty^2}{E} \cdot \left(\frac{L}{\sqrt{\frac{I_x}{A}}} \right)^3 = 12^{\frac{3}{2}} \cdot \frac{\rho_f \cdot U_\infty^2 \cdot L^3}{E \cdot h^3} \quad (3.2)$$

Van den Berg [3] designed in his research sensors with a Cauchy ratios in the range of 50.922 to 2685.4 (corrected with factor 0.12). The sensors that 'Reversed' when flow reversal was present are in the range of 407.38 to 2685.4. For this research different parameters of the sensor that result in a wider range of Cauchy ratios are designed and tested. This is to get a better overview if and how the Cauchy ratio is related to the behaviour of the sensor. The 3D printer can print with a height accuracy of 0.1 mm per layer and the sensor has to fit on the airfoil, which is 13 cm. These limits are used when determining the parameters of the sensors.

Sensors with l = 85 mm		Sensors with h = 0.3 mm			
h (mm)	Ca	l (mm)	Ca	l (mm)	Ca
0.1	31273	36.4	90.960	70.0	646.90
0.2	3909.1	40.0	120.71	80.0	965.64
0.3	1158.3	42.5	144.781	90.0	1374.9
0.4	488.64	50.0	235.75	100.0	1186.0
0.5	250.18	51.0	250.18	110.0	2510.3
0.6	144.78	60.0	407.38	120.0	3259.0
0.7	91.174	63.75	488.64	127.5	3909.1

Table 3.1: Cauchy ratios of sensors without strain gauges, the red numbers are the Cauchy ratios in the range where van den Berg's sensors bended with the flow reversal

In table 3.1 the length is fixed and the height is varied. The smallest possible heights are used as it results in a higher Cauchy ratio which indicates a sensor that will be more likely to bend with the flow, it also keeps the fabrication time to a minimum. The length of 85 mm is chosen as it results in two sensors with a Cauchy ratio above the range of 407.38 to 2685.4 and two below.

Two sensors with the same Cauchy ratio can have different structures. To investigate if the behaviour of the sensor is dependent on the Cauchy ratio or if the ratio between height and length matter, another set of sensors is made with varying lengths. As these sensors do not have a measurable output themselves, the behaviour will have to be observed using an external measurement. In this case this will be a camera and the behaviour will be visually observed from the video's. The Cauchy ratios of the designed sensors can be found in table 3.1.

3.1.2 Strain gauge

Based on the behaviour of the sensors without a strain gauge, dimension of the sensor are selected. As will be seen in chapter 5, the sensors with a height less then 0.5 mm showed a reaction in stall. To keep the sensor as thin and thus as flexible as possible a height of 0.3 mm is chosen. For the length of the sensor 70 mm is chosen. Longer sensors bend more with the flow reversal, but placement is very important for these sensors as stall extends from the tail of the wing towards the leading edge. So a longer sensor will measure stall at a higher angle then a short one. The strain gauge will be placed at the front of the sensor. If it is placed over the whole sensor then the sensor would also measure the random movements of the tail which lower the sensitivity of the sensor. This might be what happened with van den Bergs sensors [3]. Videos of the measurement with the sensors from table 3.1 showed that the sensor bends mostly in the first twenty millimetres from the sensor. So gauge lengths from 5 to 25 mm are chosen measured from the fixation point of the sensor.

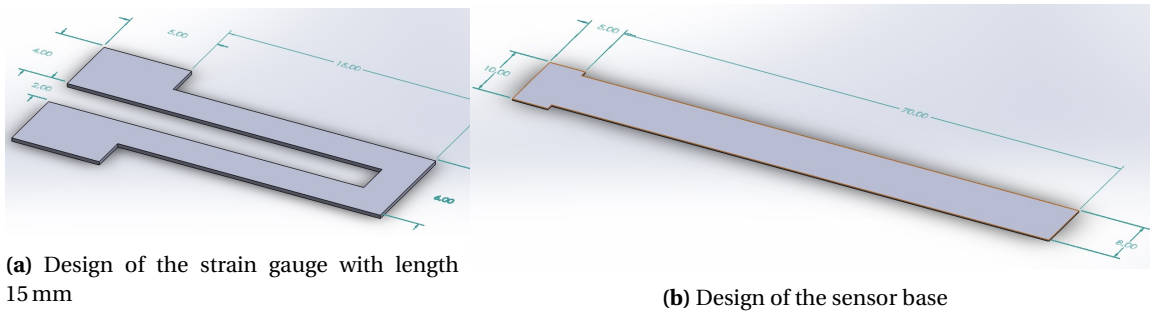


Figure 3.1: Design of the sensor

For the design of the sensor both the structures in section 2.3.1 are used. So one sensor set has a rectangular base and the other has one rectangular layer and the other layer only under strain gauge. The neutral axis of the resistors with a rectangular base is calculated using equation A.1 in the appendix and is located at 0.1346 mm from the bottom of the sensor, so in the second layer of the base. The neutral axis of the resistors with a gap is calculated using equation A.2 in the appendix and is located at 0.13 mm from the bottom of the sensor. The second moment of area of the resistors with a rectangular base is calculated using equation A.3 in the appendix and is 0.01755 mm^4 . The second moment of area of the resistors with a gap is calculated using equation A.4 in the appendix and is 0.01687 mm^4 . So the sensor with a gap has a lower neutral axis and a lower second moment of area then the sensor with a rectangular base.

The radius of gyration of the sensor is inconsistent in the length, but the Cauchy ratio is based on a consistent beam. The slenderness ratio is linearly dependent on length, so the Cauchy ratio is linearly dependent on the length to the power three. To compensate for the difference in radius of gyration the Cauchy ratio of the first part of the sensor where the strain gauge is applied is calculated. Then the length of a beam with the same structure as the tail of the

sensor (where no strain gauge is applied) and the same Cauchy ratio is calculated. So the part of the sensor with a strain gauge is substituted for a part without a strain gauge and the same Cauchy ratio. Then the Cauchy ratio of this substituted sensor is calculated.

To put it in equations, step 1:

$$Ca_{SG} = \frac{\rho_f \cdot U_\infty^2}{E} \cdot \left(\frac{l_{SG}}{r_{a,SG}} \right)^3 \quad (3.3)$$

Step 2:

$$l_{sub} = r_{a,tail} \sqrt[3]{\frac{Ca_{SG} \cdot E}{\rho_f \cdot U_\infty^2}} \quad (3.4)$$

Step 3:

$$Ca_{total} = \frac{\rho_f \cdot U_\infty^2}{E} \cdot \left(\frac{l_{sub} + l_{tail}}{r_{a,tail}} \right)^3 \quad (3.5)$$

The Cauchy ratios and the resistance measured with a 2 point measurement 3 days after printing of these sensors can be seen in table 3.2.

Length strain gauge (mm)	Rectangular sensor		Sensor with gap	
	R (kΩ)	Ca	R (kΩ)	Ca
5.0	2.01	2043.1	1.21	15158
10.0	3.0	1909.0	3.68	13062
15.0	7.6	1780.9	3.75	11169
20.0	8.1	1658.7	5.74	9468.1
25.0	7.3	1542.2	5.97	7949.4

Table 3.2: Cauchy ratios of sensors with H = 0.3 mm, L = 70 mm and different strain gauge lengths and structures

3.2 Fabrication

The sensors are made using a Diabase H-series multi-material printer [34], see figure 3.2. This printer can print with up to 5 different materials, has a height resolution of 0.1 mm and a nozzle width of 0.4 mm.

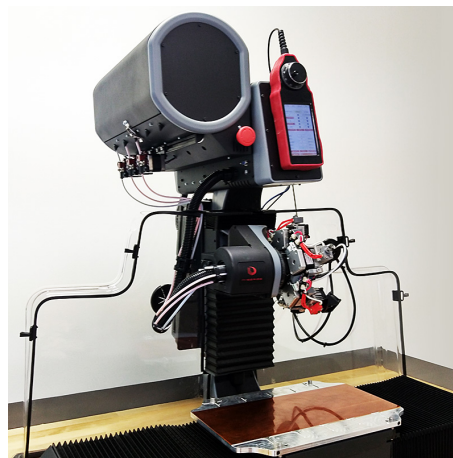


Figure 3.2: Diabase H4 Pro [35]

	Base	Strain gauge	General settings	
Material	Ninjaflex TPU	PI-ETPU 85-700		
Printing speed	15 mm s ⁻¹	15 mm s ⁻¹	Layer height	0.1 mm
Flow rate	150 %	110 %	Line width	0.4 mm
Printing temperature	205 °C	228 °C	Bed temperature	60 °C
Wall thickness	0.8 mm	0.4 mm	Enable prime tower	On
Infill density	100 %	100 %	Infill pattern	Lines
Skirt/Brim min. length	250 mm	250 mm	Build plate adhesion	Skirt

Table 3.3: Printing settings

The .stl models of the designed sensors made using the program solidworks are exported as 3D files and put into Cura [36] which slices the models. This file is then send to the 3D printer, the most important settings of the printer can be seen in table 3.3. With these settings there was no infill for the PI-ETPU, only for the base. To improve adhesion of the sensor to the build plate during printing, Kapton tape is used.

The printed sensors with strain gauge can be seen in figure 3.3. After the sensors were removed from the Kapton tape the strain gauge part curled up. This is caused by the difference in thermal expansion coefficients of the materials. This was also seen in van den Berg's research and he solved it by annealing the sensors [3]. This effect was less present during this research due to the shorter strain gauge lengths. To save time this problem was used as feature. When the sensor is in a laminar attached flow, the airflow is expected to push the sensor to the airfoil and the strain gauge will be flattened.



Figure 3.3: Printed sensors with strain gauge on the Kapton tape

The wires can not directly be soldered onto the sensors as the soldering temperature is higher than the melting temperature of the sensor. So the contacts of the sensors with a strain gauge are placed by using copper tape and silver ink. First the wires are soldered onto the copper tape, then the tape is placed on the sensor and lastly the silver ink is applied to the copper tape and the sensor to decrease the contact resistance.

3.3 Conclusion

In this chapter the design choices and fabrication process of sensors with and without strain gauges are explained.

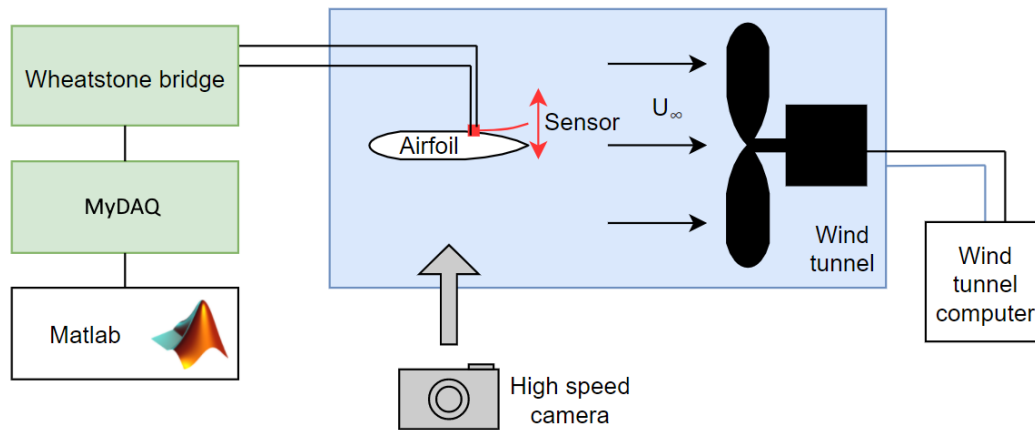
The sensors with a gap have a lower neutral axis, lower second moment of area and higher Cauchy ratio than the sensors with a rectangular base, so according to this they should work better. The results will have to show if the sensor with a gap in the base works indeed better.

4 Method

In this chapter the different components of the test set-up are introduced and the methodology of how the measurements will be carried out are described. This will be used to test the sensors that are designed in chapter 3.

4.1 Test set-up

The sensor is tested in a wind tunnel, the mechanical behaviour of the sensor will be observed using a camera and the electrical behaviour of the sensor with strain gauge will be measured using a Wheatstone bridge and a MyDAQ. The test set-up can be seen in figure 4.1.



(a) Schematic of the test set-up [3]



(b) Photo of the test set-up

Figure 4.1: Test set-up for the sensor

4.1.1 Wind tunnel

The sensor is tested in an Educational Wind Tunnel (EWT) designed by Aerolab [37]. This wind tunnel can control the angle of attack and the free stream velocity. The sensors are placed on a NACA 0012 airfoil using double sided tape. The airfoil will be placed in a wind tunnel. There were three sizes of this airfoil printed, all three with a span width of 20 cm, the cord lengths of the airfoils are 10 cm, 12 cm and 14 cm. The sensors from table 3.1 exceed the length of two of these airfoils and can only be tested on the 14 cm cord length air foil. Due to an unfortunate

incident described in section 4.1.2 the sensors with $l = 85$ mm from table 3.1 are tested on the 10 cm cord length air foil. The prints with $h = 0.3$ mm from table 3.2 are tested on the 12 cm cord length air foil.

4.1.2 Camera

For the visual observation of the sensor the Casio Exilim EX-F1 [38] is used. This camera has a high speed function which is used to make video's of 2 seconds with a frame rate of 300 fps. Because of this high frame rate, the camera needs more light. So an industrial LED lamp is used. This was first a halogen lamp, but it heated up very much and very fast. This destroyed the 3D printed airfoil made from PLA, which has a glass transition temperatures between 50°C and 80°C [39]. This caused the prints from table 3.1 to be measured on another airfoil then the prints from table 3.1.



Figure 4.2: Warped airfoil after being placed under a halogen lamp

4.1.3 Wheatstone bridge

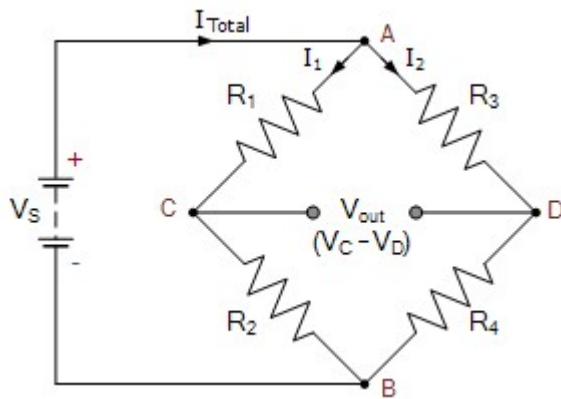
The resistance of the strain gauge will be measured using a Wheatstone bridge. A Wheatstone bridge is a circuit that consists of two parallel voltage dividers. The output of the circuit is the difference in output of the voltage dividers. Three of the four resistors in this set-up are known (R_1 , R_2 and R_3), the fourth will be the strain gauge (R_4). The Wheatstone bridge is most sensitive to resistance changes when the values of the fixed resistors are close to the value of the changing resistance. The resistances of the sensors varies from 1.2 to 8.1 k Ω , see table 3.2. So $R_1 = R_2 = R_3 = 5$ k Ω is chosen. The circuit diagram can be seen in figure 4.3 and the equation for the output of the circuit can be seen in equation 4.1.

$$V_{\text{out}} = V_S \cdot \left(\frac{R_2}{R_1 + R_2} - \frac{R_4}{R_3 + R_4} \right) \quad [40] \quad (4.1)$$

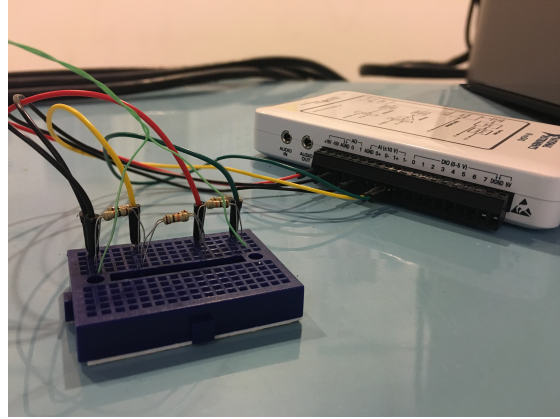
The circuit will be monitored by a myDAQ [41]. The input of the circuit will be connected to a 15 V output of the myDAQ and the output will be measured using the data logger function of the myDAQ. The measured voltage can be translated into the strain gauge resistance by rewriting equation 4.1 to equation 4.2.

$$R_4 = R_3 \frac{R_2 \cdot V_{\text{in}} - (R_1 + R_2) \cdot V_{\text{out}}}{R_1 \cdot V_{\text{in}} + (R_1 + R_2) \cdot V_{\text{out}}} \quad (4.2)$$

Using the 34401A Digital Multimeter [42] a two point measurement was done to verify the resistor values and the voltage output of the myDAQ. These values were: $R_1 = 4.94$ k Ω , $R_2 = 4.95$ k Ω ,



(a) Schematic of a Wheatstone Bridge [40]

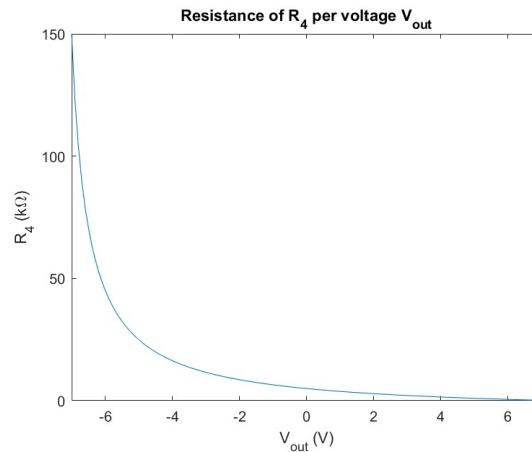


(b) Photo of the Wheatstone Bridge connected to the myDAQ

Figure 4.3: Test set-up for the Wheatstone bridge

$R_3 = 4.95 \text{ k}\Omega$ and $V_{in} = 14.974 \text{ V}$. This gives equation 4.3 and the corresponding graph for the output in figure 4.4. In this figure it can be seen that a difference in a higher voltage has a smaller range of corresponding resistances than the lower voltages. So lower resistances can be measured more accurately than the higher resistances in this particular set-up. The resistances range of the sensor, from 1.2 to 8.1 $\text{k}\Omega$, corresponds to a voltage range of -1.8 to 4.6 V.

$$R_4 = \frac{74121.3}{V_{out} + 7.47943} - 4950 \quad (4.3)$$

**Figure 4.4:** The output of the Wheatstone bridge against the corresponding resistance of the strain gauge

The analog input channel of the myDAQ is used with sampling frequency $f_s = 1 \text{ kHz}$. This channel has an ADC resolution of 16 bits and a range of $\pm 10 \text{ V}$ [43], so assuming all voltage steps between bits are equal the accuracy is $\frac{20}{2^{16}} = 0.31 \text{ mV}$. With $f_s = 1 \text{ kHz}$ the settling error is $\approx 0.05 \%$ [43]. So with the higher resistance of 8.1 $\text{k}\Omega$, the smallest resistance change that can be measured is $R_{4, v=-1.8003} - R_{4, v=-1.8} = 8101.5356 - 8100.8343 = 0.701 \Omega$. This is very small compared to the resistance of the sensor, so the significant errors in the signal will be from noise and not from the measurement set-up.

4.2 Measurement methodology

Two types of measurements will be done, one where the relation between the Cauchy ratio and the aeroelastic behaviour of the sensor in stall is investigated and one where the performance of the designed sensors is investigated.

4.2.1 Cauchy ratio as function of behaviour in stall

The sensor is applied to the airfoil using double sided tape and will be placed as much to the tail of the airfoil as possible, so the tail of the airfoil and the tail of the sensor at the same place. This is done since stall first occurs here. For the longer sensors, when stall first occurs only part of the sensor is in stall. The normal and axial forces that are measured by the wind tunnel computer will be saved for the angles 11° through 15° with steps of 0.5° . Van den Berg's research showed that under the same test circumstances stall occurs in this range [3]. These forces are used to calculate the lift and coefficient and prove that the behaviour is indeed observed in stall. Three data points are saved per angle to minimize the deviation from the accurate value's, the average of these points are used for the calculations.

During this measurement video's of the behaviour of the sensor are made for roughly 2 seconds with the camera when the free stream velocity is 10 ms^{-1} . The sensors will be marked with a pen stripe every centimetre, this is to better evaluate the bending of the sensor and to find the optimal length for a strain gauge.

It is expected that the sensors with higher Cauchy ratios will move more then the sensors with lower Cauchy ratios. So the data will be analysed by categorizing the different behaviours of the sensors in stall. The output of the wind tunnel computer will be used to confirm stall occurs.

4.2.2 Strain gauge

This measurement is also done with the relative velocity of the wind tunnel at 10 ms^{-1} . The angle of attack is varied from 11° through 15° with steps of 1° , 1° and 20° are also measured as reference points for when the flow is laminar (1°) and the flow is turbulent (20°).

The sensors with a strain gauge will also be applied using double sided tape and placed as much to the tail of the airfoil as possible. At everyone of these angles the output of the Wheatstone bridge, forces on the airfoil and videos of the behaviour are measured/taken. The output of the Wheatstone bridge is measured by the myDAQ for at least 10 seconds. The forces on the airfoil are measured by the wind tunnel computer and again three data points are saved per angle. The video's of the behaviour of the sensor will be taken for roughly 2 seconds.

It is expected that the sensor will decrease in resistance as the angle of attack increases. When the angle of attack increases, then stall will occur at the trailing edge expanding towards the leading edge. This will increase bending of the sensor, which increases the compression of the strain gauge and will result in a decrease in resistance. So the measured voltage will be converted to resistance and the resistance outputs of different angels will be compared.

4.3 Conclusion

The sensors are tested in the wind tunnel using the wind tunnel computer and a high speed camera. The sensors with a strain gauge are also measured using a Wheatstone bridge and a MyDAQ. The measurement and analysis methodology are explained in section 4.2.

5 Results

The designed sensors from chapter 3 are tested using the methods from chapter 4. In this chapter the results of these measurements are presented and summarized. The behaviour of the sensors without a strain gauge in stall are categorized. The resistance of the sensors with a strain gauge are analysed based on their DC and AC behaviour.

5.1 Cauchy ratio as function of behaviour in stall

The sensors without a strain gauge were tested on different airfoils, see section 4.1.1. The lift coefficient versus the angle of attack versus the drag coefficient of these different airfoils can be seen in figure 5.2. The airfoil with a 10 cm cord line has a seemingly random lift coefficient. No clear angle of attack from which stall occurs can be derived from these figures. For the airfoil with a 14 cm cord line holds that the angle of attack at which stall occurs is also hard to derive from the figures. However, it can be seen that the sensors with a length greater than 90 mm produce significantly more drag than the shorter sensors. From the video's can be derived that for both airfoils stall occurs around 12.5° and 13° , this is where the sensors start to show movement. So when the behaviour of the sensors at $AoA = 15^\circ$ is observed, then this is indeed in stall.

The visually observed behaviour of the sensors without a strain gauge in stall can be seen in table 5.1 and 5.2. The behaviour is categorized in four types: nothing, flapping, planking and bending. Nothing is used when the sensor lays on the airfoil and does not move. Flapping is used when the sensor is moving while it stays close to the airfoil, distance between airfoil and sensor <0.5 cm. Planking is used when the sensor only bends at the place of attachment and bending is when the sensor itself also bends. When the sensor switches between behaviours, then both behaviours are mentioned. These behaviours can be seen in figure 5.1. Due to the time consuming nature of the categorizing, there was chosen to only do the analysis in stall and use the remaining time to analyse the sensors with a strain gauge.

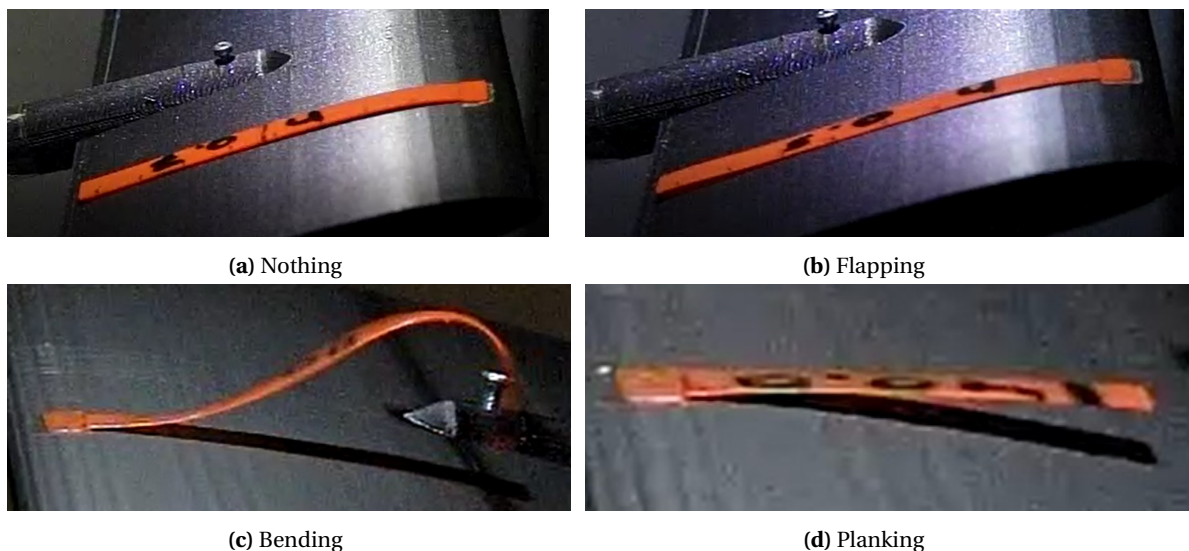


Figure 5.1: Behaviour categories

It is worth noting that the sensors with $l = 85$ mm, $h = 0.6$ mm and $h = 0.7$ mm do not move while the Cauchy ratio is above 60, far more than 1.

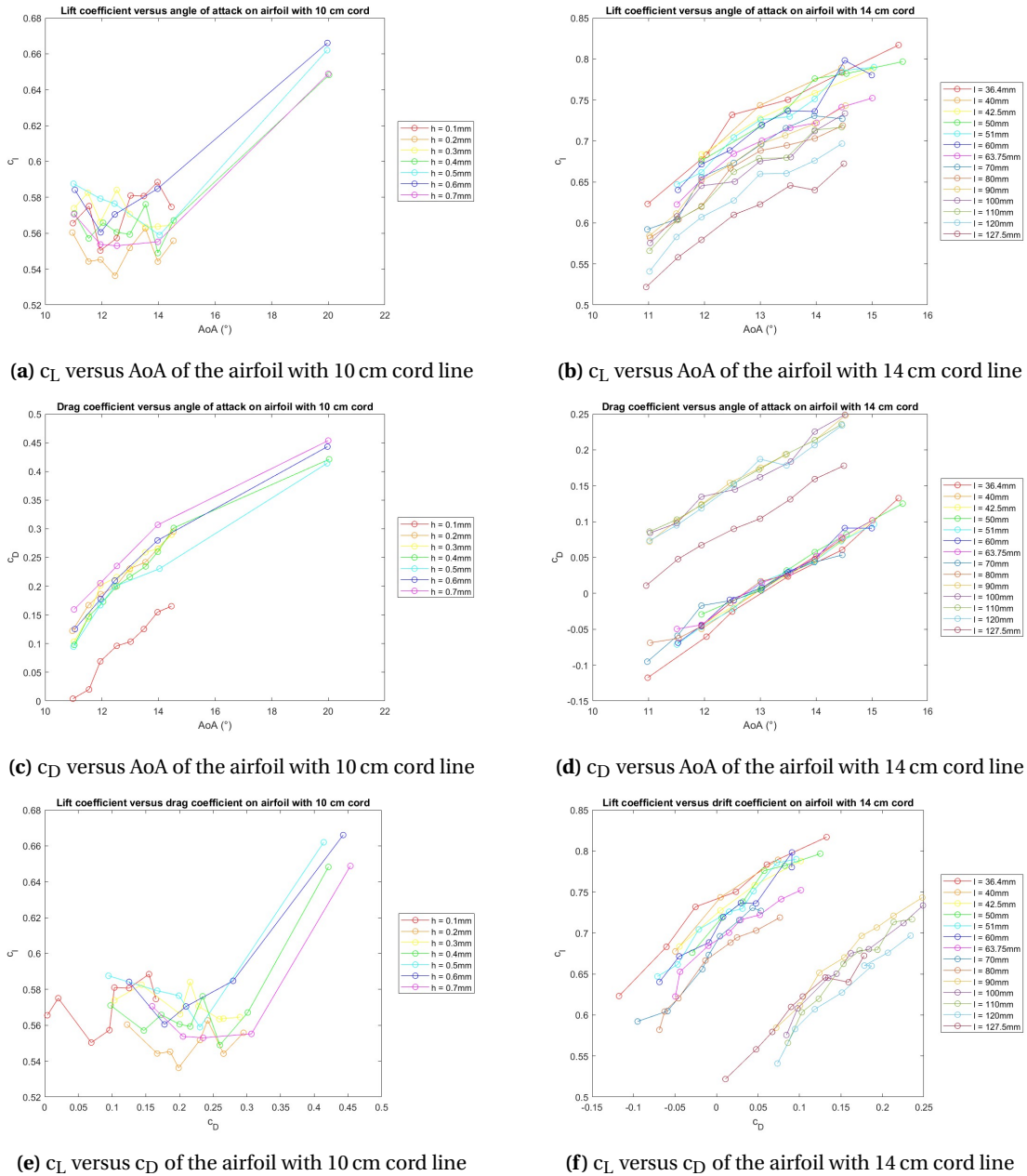


Figure 5.2: Airfoils on which the sensors without a strain gauge were tested

5.2 Strain gauge

The lift coefficient versus the angle of attack versus the drag coefficient of the airfoil with a 12 cm cord line can be seen in figure 5.3. By comparing the lift and drag coefficients at certain angles it can be seen that the drag coefficient starts to increase faster than the lift coefficient at $AoA > 12^\circ$, so this is where stall occurs.

The ten designed sensors were all tested in the wind tunnel. The output of two of the sensors can be seen in figure 5.4. Out of the ten sensors these two are shown because the results per sensor are very different. The sensor with a gap and a strain gauge length of 15 mm in figure 5.4b shows very good results, both the average of the sensor and the deviation from this average changes with the angle of attack. The rectangular sensor with a strain gauge length of 5 mm however has a very high rest resistance in contrast to the output when the wind tunnel is on. For $AoA = 1^\circ$ the output shows jumps between two averages which could indicate unsta-

Sensors with $l = 85$ mm		
h (mm)	Ca	Behaviour in stall
0.1	31273	Bending
0.2	3909.1	Bending
0.3	1158.3	Bending
0.4	488.64	Flapping
0.5	250.18	Flapping
0.6	144.78	Nothing
0.7	91.174	Nothing

Table 5.1: Behaviour of the sensors without a strain gauge at $\text{AoA} = 15^\circ$ and $U_\infty = 10 \text{ ms}^{-1}$

Sensors with $h = 0.3$ mm					
l (mm)	Ca	Behaviour in stall	l (mm)	Ca	Behaviour in stall
36.4	90.960	Planking	70.0	646.90	Bending
40.0	120.71	Planking	80.0	965.64	Bending
42.5	144.78	Planking	90.0	1374.9	Bending
50.0	235.75	Planking, Bending	100.0	1186.0	Flapping, Bending
51.0	250.18	Planking, Bending	110.0	2510.3	Flapping, Bending
60.0	407.38	Bending	120.0	3259.0	Bending
63.75	488.64	Bending	127.5	3909.1	Flapping, Bending

Table 5.2: Behaviour of the sensors without a strain gauge at $\text{AoA} = 15^\circ$ and $U_\infty = 10 \text{ ms}^{-1}$

ble contacts. To investigate these behaviours further a DC and an AC analysis are done. The remaining figures with the resistance of the sensor over time can be found in appendix B.1.

5.2.1 DC change

For the DC analysis the mean of the resistances per angle are calculated. Different kinds of behaviours are obtained from this analysis.

The sensor with a rectangular base and a strain gauge length of 5 mm, 10 mm and 15 mm and the sensors with a gap in the base and a strain gauge length of 20 mm show a decrease in resistance when the angle of attack increased. But the resistance increases after the angle of attack has reached 15° and the resistance when the wind tunnel is off is higher than when the wind tunnel is on. An example of this behaviour can be seen in figure 5.5.

The sensor with a rectangular base and a strain gauge length of 20 mm and the sensors with a gap in the base and a strain gauge length of 5 mm and 25 mm each showed unique behaviour. The sensor with a rectangular base and a strain gauge length of 20 mm shows the same as in figure 5.5 but has a resistance when the wind tunnel is off in the same range as when the wind tunnel is on. The sensors with a gap in the base and a strain gauge length of 5 mm shows the same as in figure 5.5 but the increase in resistance starts after the angle of attack has reached 12° . The sensors with a gap in the base and a strain gauge length of 25 mm is the only sensor that shows an increased resistance for an angle of attack between 12° and 14° . The means of these sensors can be seen in figure 5.6.

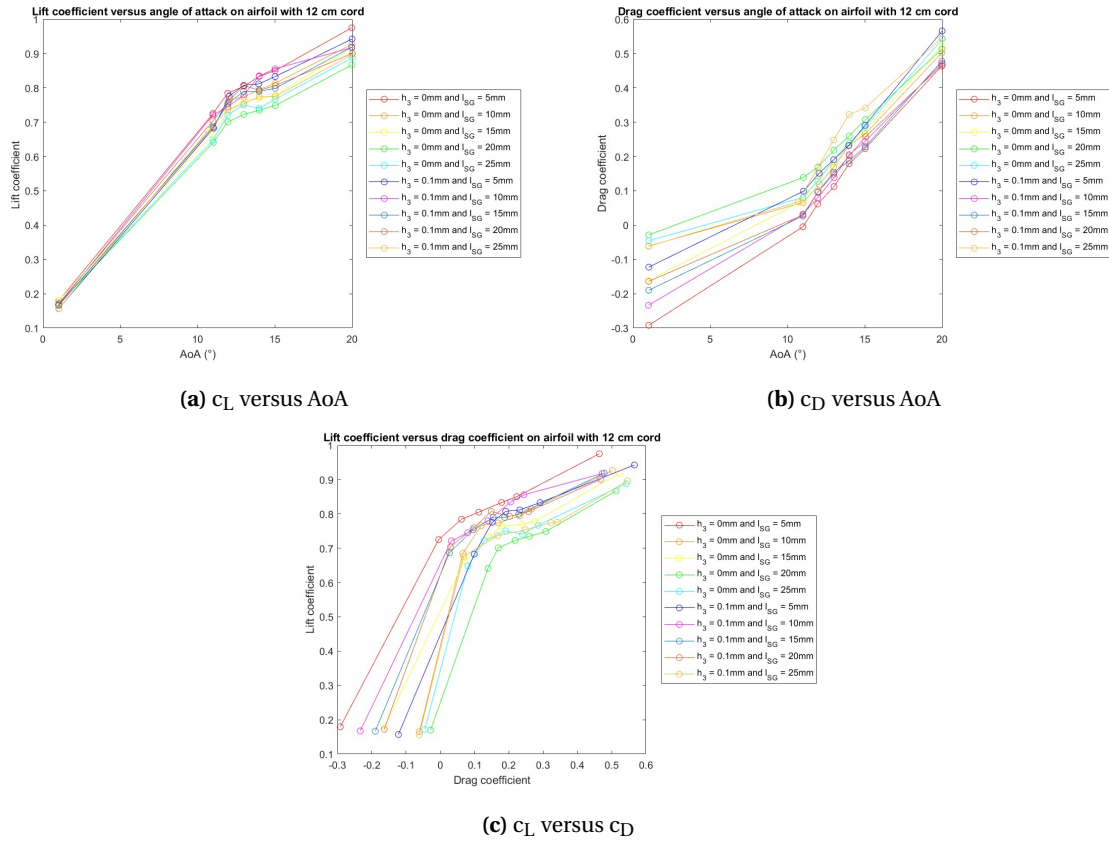


Figure 5.3: Airfoil on which the sensors with a strain gauge were tested

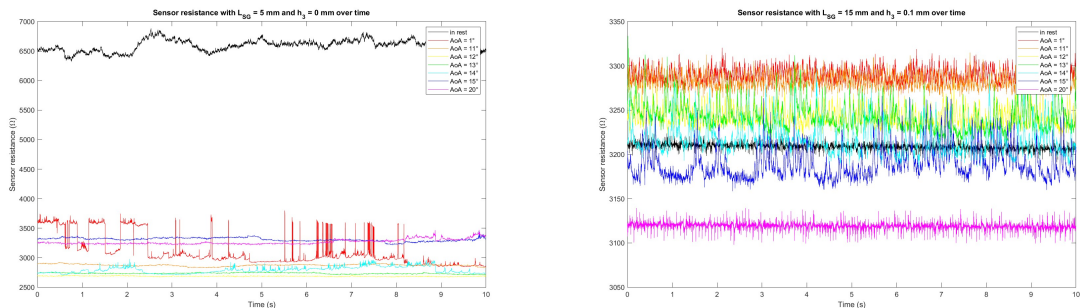


Figure 5.4: Output of the sensors in resistance at different angles of attack

The last type of behaviour are sensors with a continuing drop in resistance as the angle increased and a resistance when the wind tunnel is off in the same range as when the wind tunnel is on. These are the sensor with a rectangular base and a strain gauge length of 25 mm and the sensors with a gap in the base and a strain gauge length of 10 mm and 15 mm. An example of this behaviour can be seen in figure 5.7.

To investigate if the high resistance when the wind tunnel is off compared to the resistance when the wind tunnel is on is caused by the contacts a 4 point measurement was done and compared to a 2 point measurement. The sensors with a strain gauge length of 25 mm are not tested again as the contacts broke off. The results can be seen in table 5.3. When the resistance fluctuates with differences more than 0.5 kΩ, then the maximum and minimum are noted.

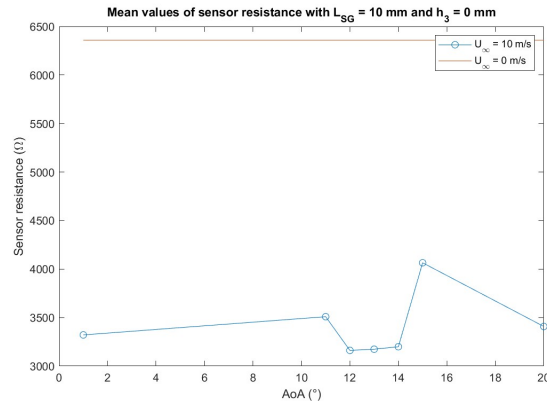
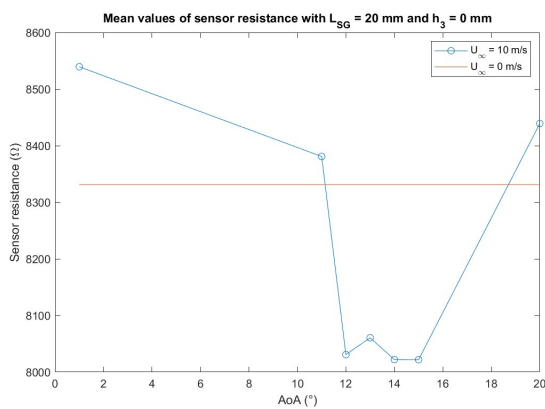
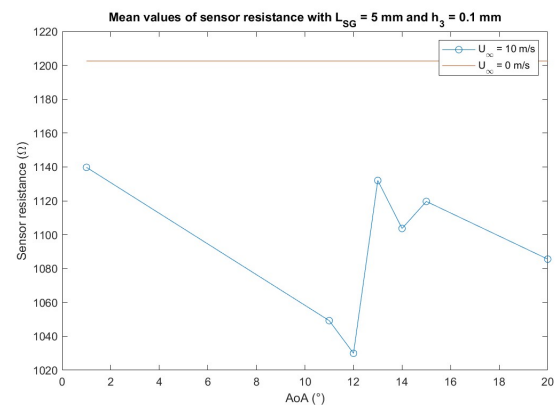


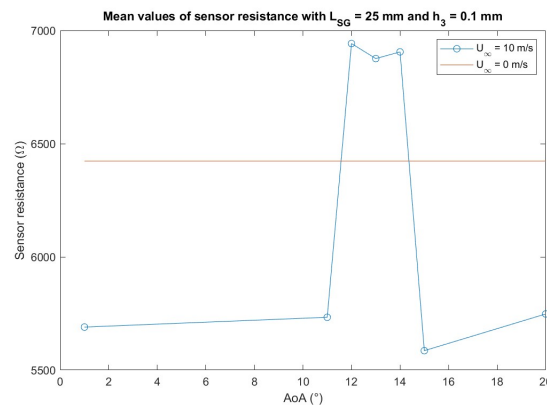
Figure 5.5: Drop in resistance followed by an increase and high rest resistance



(a) Rectangular sensor with a strain gauge length of 20 mm



(b) Sensor with a gap and a strain gauge length of 5 mm



(c) Sensor with a gap and a strain gauge length of 25 mm

Figure 5.6: Mean resistances of sensors at different angles of attack

During the testing it was noticed that when the angle of attack was changed while the wind tunnel was off the resistance also changed. This happened because the wires are fixed as they leave the wind tunnel, so when the angle is changed the force on the wires and thus on the contacts also changed. To investigate this change in contact resistance, the sensor was also tested on all angles with the wind tunnel off. This test was done using the same measurement methodology as when the wind tunnel is on with only difference that the wind tunnel is off. The results of this measurement compared to the initial measurement can be seen in figures 5.8.

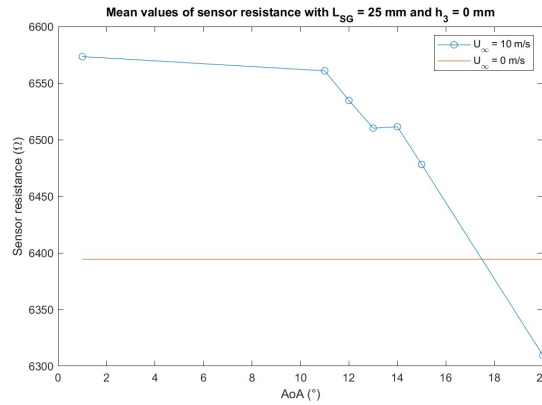
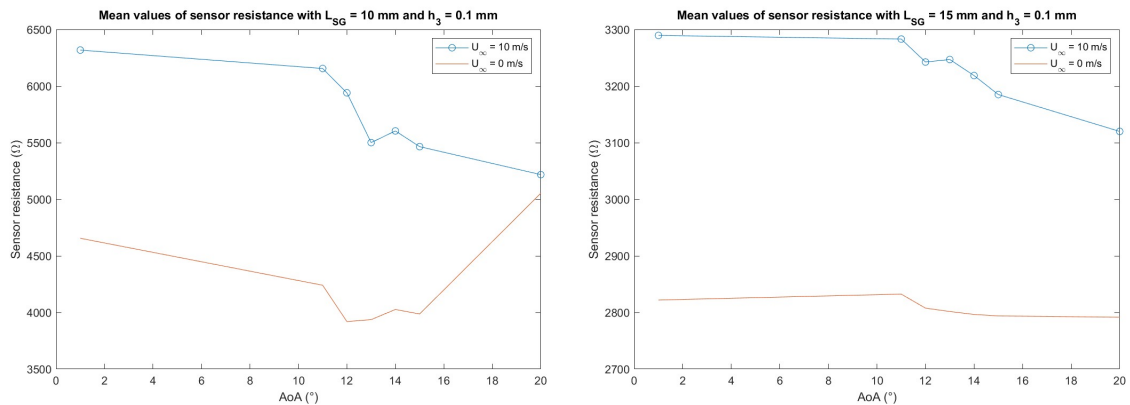


Figure 5.7: Continuing drop in resistance

Length strain gauge (mm)	Rectangular sensor		Sensor with gap	
	R ₂ -point (kΩ)	R ₄ -point (kΩ)	R R ₂ -point (kΩ)	R ₄ -point (kΩ)
5.0	10 - 1000	1.7	0.9 - 100 000	1.12
10.0	40 - 100	2.4	2.7 - 3.7	2.3
15.0	5 - 200	4.4	2.6 - 3.3	2.4
20.0	7.6	6-5.5	3.8 - 200	4.0

Table 5.3: two and four point measurements of sensors with a strain gauge

The sensor with a rectangular base and a strain gauge length of 25 mm was not tested again as the contacts broke off.



(a) Sensor with strain gauge length 10 mm

(b) Sensor with strain gauge length 15 mm

Figure 5.8: Mean of the resistance per angle of sensors with gap with the wind tunnel on and off

These results show overall a lower resistance, this is caused by the changing resistance of PI-ETPU, see section 2.2, and a difference in contact resistance caused by the placing and removing of the sensor on the airfoil and the container in which the sensors are kept. During the initial tests a reference resistance was measured an angle of attack of 11° with the wind tunnel off. The ratio between the mean of this resistance and the mean of the resistance measured at AoA = 11° at the second test is used to correct the difference in means. By doing this there is assumed that all unknown factors that influence the resistance of the sensor at other angles

then 11° have the same ratio between the initial test and the second test. The adjusted means can be seen in figure 5.9.

$$\text{Mean}(R_{\text{test1, approx}}) = \text{Mean}(R_{\text{test2}}) \cdot \frac{\text{Mean}(R_{\text{test1, AoA} = 11^\circ})}{\text{Mean}(R_{\text{test2, AoA} = 11^\circ})} \quad (5.1)$$

Figure 5.9a shows a change in contact resistance similar to the resistance changes in figure 5.6a.

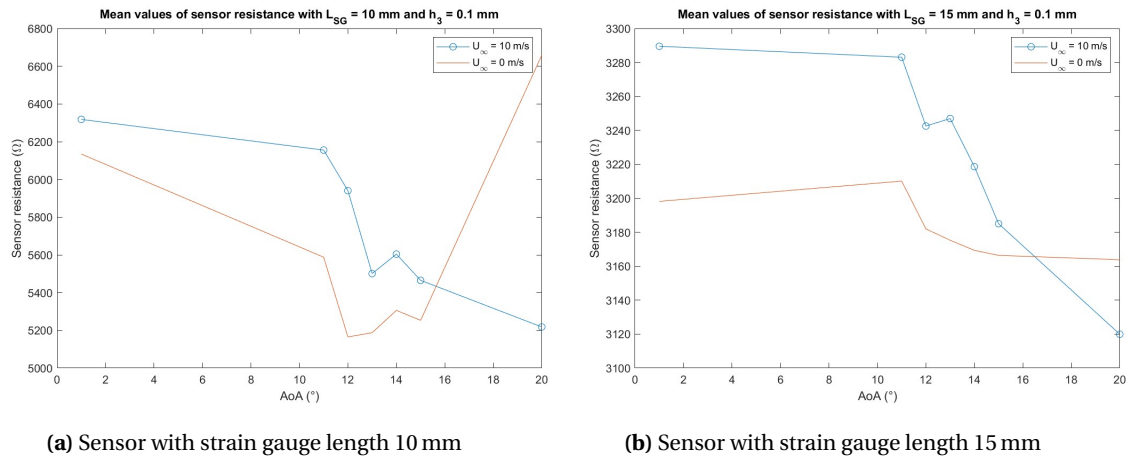


Figure 5.9: Adjusted mean of the resistance per angle of sensors with gap with the wind tunnel on and off

The resistance changes for when the wind tunnel is off and when it is on show some similarities in their course. To filter out these similarities the difference between the resistance when the wind tunnel is on and when the tunnel is off is calculated. The result can be seen in figure 5.10. There is a decrease in resistance in stall visible, but the resistance of $\text{AoA} = 12^\circ$ stands out in both graphs.

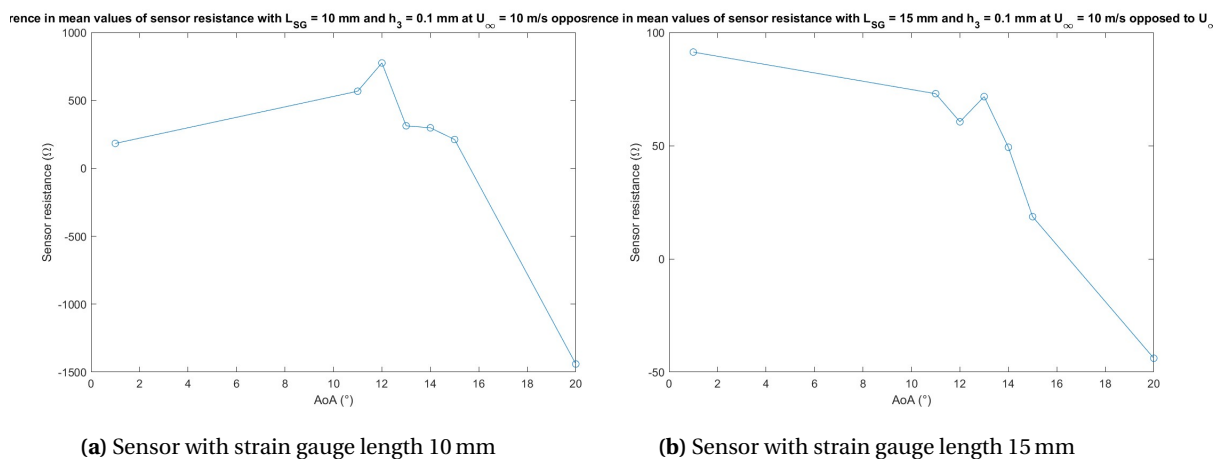


Figure 5.10: Difference in adjusted means of the resistance per angle of sensors with gap with the wind tunnel on and off

All of the figures with the resistance mean per angle of attack can be found in appendix B.2.

5.2.2 AC change

The frequency spectrum of the resistance is similar for all of the sensors, an example can be seen in figure 5.11. All of the frequency spectra can be found in appendix B.3.

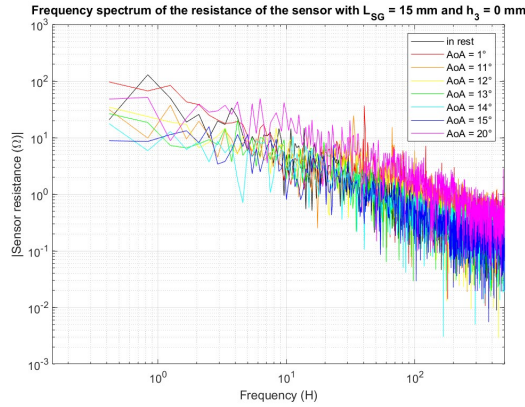
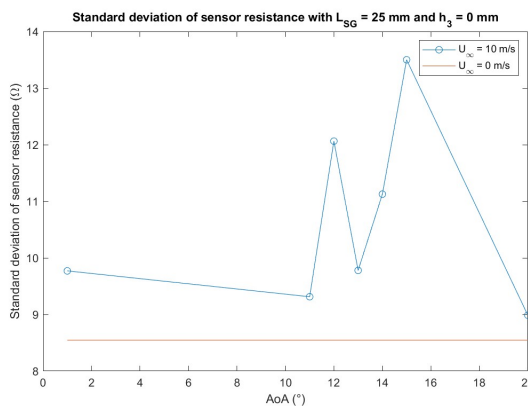


Figure 5.11: Frequency spectrum of the resistance of a sensor

The flapping of the sensors does not happen at one specific frequency, so to observe the AC behaviour of the sensor the standard deviation of the resistance is better than the frequency spectrum. Standard deviation is also dependent on the mean of the signal and in section 5.2.1 it was seen that this differs per angle. So a high pass filter is used to filter out the DC part of the signal. The cut off frequency of this filter is set to 1 Hz, at this frequency the DC part at 0 Hz is filtered out and it is low enough to still have a significant part of the output. After this filter, the standard deviation of the resistance of the sensor per angle is calculated.

These standard deviations per angle of attack show different kinds of behaviours. The results can be put in two groups, those with deviations below 40 Ω and those with deviations up to 160 Ω.

The sensor with a rectangular base and a strain gauge length of 25 mm and the sensors with a gap in the base and a strain gauge length of 5 mm, 15 mm and 25 mm have deviations below 40 Ω. They also show peaks in deviation from an angle of attack of 11° up to 15° and then a drop when the angle of attack is 20°. They also have a standard deviation when the wind tunnel is off is lower than when the wind tunnel is on. An example of this behaviour can be seen in figure 5.12a.



(a) Peaks in standard deviation for AoA = 11° - 15°



(b) Sensor with a gap and strain gauge length of 5 mm at AoA = 20°

Figure 5.12: Behaviour of majority of the sensors

The rectangular sensor with a strain gauge length of 20 mm and the sensors with a gap and a strain gauge length of 10 mm have the same behaviour but with deviations up to 160 Ω.

These six sensors had in common that at an angle of attack of 20° the sensors was stuck in a curled up position, see figure 5.12b. This is probably what caused the drop in standard deviation at this angle.

The rectangular sensor with a strain gauge length of 5 mm and 15 mm show drops in standard deviation from an angle of attack of 11° up to 15° and have deviations up to 160Ω . In these graphs the standard deviation of the resistance is higher when the wind tunnel is off then when it is on for at least four out of the seven tested angles. An example of this behaviour can be seen in figure 5.13.

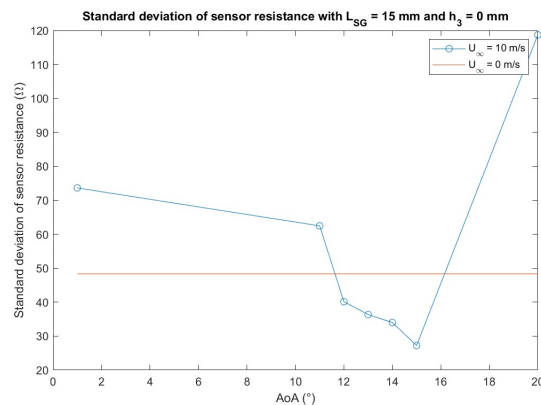


Figure 5.13: Drops in standard deviation for AoA = 11° - 15°

The rectangular sensor with a strain gauge length of 10 mm has a drop in standard deviation at an angle of attack of 12° and a peak at 14° . See figure 5.14.

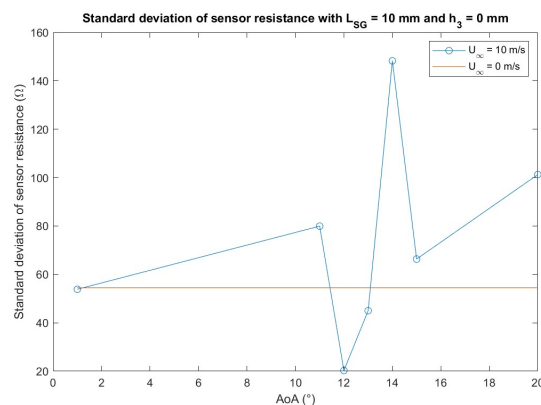


Figure 5.14: Drops in standard deviation at AoA = 12° and peak at 14°

The sensors with a gap and a strain gauge length of 20 mm has an increasing standard deviation with the angle of attack and deviations up to 160Ω . See figure 5.15.

All standard deviation of the resistance of the sensors after the high pass filter can be found in appendix B.4.

The second test with the sensors with a gap and a strain gauge length of 10 mm and 15 mm where the output of the sensors is tested on different angles with the wind tunnel off are also used to investigate the difference in standard deviation caused by the changing of the angle. These results can be seen in figure 5.16. The standard deviation of the sensor resistance does not change significantly when the wind tunnel is of and the angle is changed.

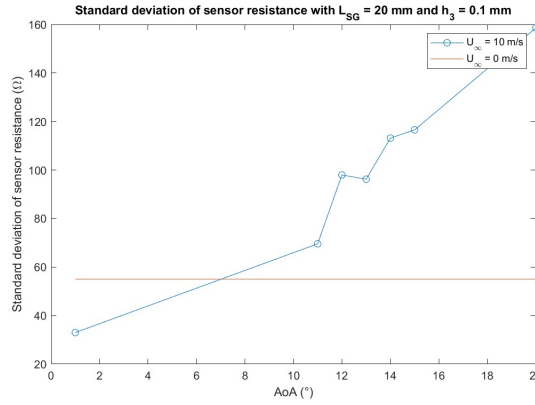


Figure 5.15: Increasing standard deviation with angle of attack

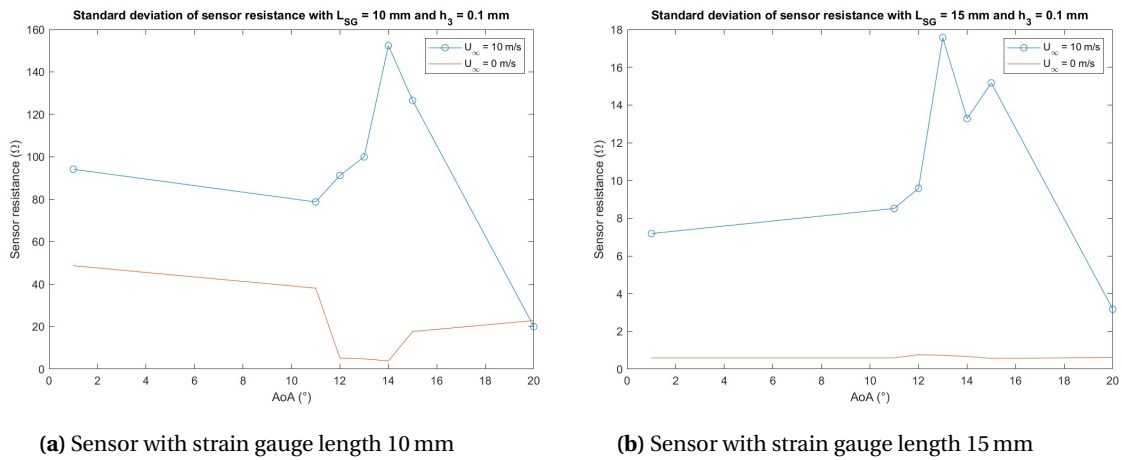


Figure 5.16: Standard deviation of the resistance per angle of sensors with gap with the wind tunnel on and off

For these results the difference between the first and second test are compensated using the same method as the DC analysis. See equation 5.2 and figure 5.17.

$$\text{Std}(R_{\text{test1, approx}}) = \text{Std}(R_{\text{test2}}) \cdot \frac{\text{Std}(R_{\text{test1, AoA} = 11^\circ})}{\text{Std}(R_{\text{test2, AoA} = 11^\circ})} \quad (5.2)$$

5.3 Conclusion

The behavior of the sensors without a strain gauge are categorized in four types: nothing, flapping, planking and bending. When stall occurred during these measurements could not be derived from the lift and drag coefficients, so the behaviour of the sensors at different angles were used to determine this.

The sensors with a strain gauge are analysed based on their mean at different angles, both with the wind tunnel off and on. The AC behaviour of the sensors is analysed based on their standard deviation per angle of attack after a 1 Hz high pass filter.

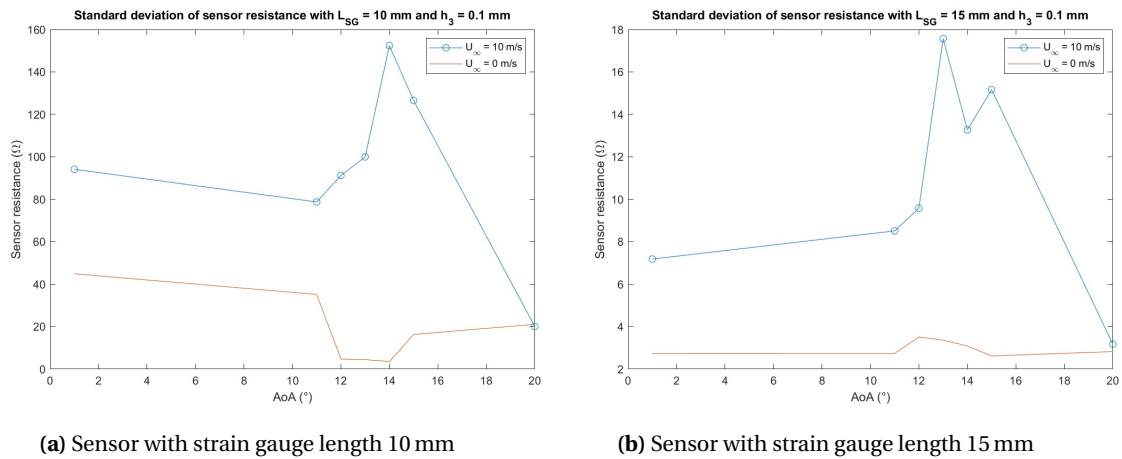


Figure 5.17: Adjusted standard deviation of the resistance per angle of sensors with gap with the wind tunnel on and off

6 Discussion

In this chapter the conclusions from chapter 2, the measurement set-up as described in chapter 4 and the results from chapter 5 are evaluated. Recommendations for follow-up research and how to optimize the sensors are done.

6.1 Mechanical properties of the sensor

In chapter 2, some mechanical properties of the sensor are evaluated, the neutral axis and the second moment of area. But these are not the only mechanical properties relevant to the sensor. A further, more extensive analysis of these properties can be done to gain more understanding of the functioning of the sensor. This might be interesting for future research.

6.2 Method

For the measurements three different airfoils are used, one for the sensors without a strain gauge and lengths of 85 mm, one for the sensors without a strain gauge and heights of 0.3 mm and one for the sensors with a strain gauge. This makes comparing the sensors based on their aeroelastic behaviour complicated as the aerodynamics of the airfoils are different.

The placement of the sensors on the airfoils also influence the results as stall first occurs at the trailing edge. So sensor that are longer or placed more towards the leading edge than other sensors are also more complicated to compare based on aeroelastic behaviour.

The Wheatstone bridge that is used to measure the resistance of the sensors with a strain gauge consists of the same resistances for every test. This results in a lower sensitivity for the sensors with a higher resistance.

These set-ups influence the results and should be taken into account when evaluating them.

6.3 Results

The results are discussed per sensor and per type of analysis. So first the tests with the sensors without a strain gauge are discussed. Then the DC analysis of the sensors with a strain gauge are discussed and lastly the AC analysis of the sensors with a strain gauge are discussed.

For all results hold that with a higher resolution video's the behaviour of the sensors could be analysed using point tracking software. This can be useful in comparing results and is therefore recommended for further research.

6.3.1 Cauchy ratios as function of behaviour in stall

In chapter 5, it could be seen that the sensors with a length greater than 90 mm produce significantly more drag than the shorter sensors. As for the behaviour of the sensors, planking only occurs to the shorter sensors ($l = 36.4$ mm to $l = 51$ mm, they are lighter than the sensors with the same Cauchy ratio but bigger dimensions. The sensors with the Cauchy ratios 250.18 and 488.64 also show different behaviour for different dimensions, where the shorter and thinner sensors bend the longer and thicker ones only flap. In both cases the heavier sensors show less movement, so gravity could play in a roll in this effect. For the higher Cauchy ratios this effect seems to be less significant as the sensors with a Cauchy ratio above 1158.3 all show the behaviour of bending. A flow sensor with a Cauchy ratio above this value is thus best as it shows the most movement and thus has the most significant output. But if the sensor is made with even bigger parameters then tested in this research, less movement could occur. A follow-up research to investigate the relation between the aeroelastic behaviour and the Cauchy ratio could be done by testing more sensors with different dimensions and the same Cauchy ratio.

Another follow-up research into the effect of gravity on the behaviour of these sensors could be done, for example by testing sensors placed on the bottom and on the top of the airfoil and comparing their behaviour.

6.3.2 DC resistance change in sensors with a strain gauge

In section 5.2.1 different types of DC behaviour are seen. In table 5.3 it can be seen that some sensors have differences of less than 1 k Ω between the four and two point resistance measurements while others have differences ranging up to multiple hundreds of kilo ohms. The sensor with a rectangular base and a strain gauge length of 5 mm, 10 mm and 15 mm and the sensors with a gap in the base and a strain gauge length of 5 mm and 20 mm are those with the differences ranging up to multiple hundreds of kilo ohms. These sensors are also the only ones with a higher mean resistance value when the wind tunnel is off than when the wind tunnel is on. So it can be concluded that this high resistance is caused by the contact resistance. To minimize the effect of these contact resistances a four point measurement during testing can be used in follow-up researches.

The sensor with a rectangular base and a strain gauge length of 5 mm, 10 mm and 15 mm and the sensors with a gap in the base and a strain gauge length of 20 mm all showed the same pattern in their mean resistance per angle of attack, see figure 5.5. This pattern is similar to the pattern of the resistance when the wind tunnel is off per angle of attack seen in figure 5.9a. This could indicate that for these sensors, the mean difference is caused by the contact resistance at different angles in the wind tunnel.

Three of the remaining sensors show a consistent drop in resistance per angle of attack. These are the sensor with a rectangular base and a strain gauge length of 25 mm and the sensors with a gap in the base and a strain gauge length of 10 mm and 15 mm. After testing the contact resistance per angle of attack with the wind tunnel off, it can be seen that part of this resistance drop is caused by the difference in contact resistance at different angles in the wind tunnel, see figure 5.8. After correction of this, a resistance drop during stall was still seen, see figure 5.10. The remaining change in the mean of the resistance can be caused by the angle of attack, and thus the difference in bending of the sensor, or by unknown factor that were not taken into account for the correction, e.g. difference in temperature.

From these results no clear limitations can be derived as to what sensor structure gives a certain DC output. There is however a clear relation in table 5.3 between resistance and strain gauge length. The longer sensors have a higher resistance, which was to be expected based on the equation for resistance seen in eq. 2.1.

To investigate the relation between the angle of attack and the DC output of the sensor more accurately different ways to attach the contacts could be used, such as increasing the surface the copper tape is placed on or using an entire different technique. This could be for example, printing the contact pads with only PI-ETPU and melting the wires into the material using a soldering iron. By making more of the same sensors and testing those, unknown factors caused by a deviating sensor can be averaged out. The sensor could also be tested on more different angles before and after stall occurs to see if there are patterns in the sensor behaviour on other angles.

6.3.3 AC resistance change in sensors with a strain gauge

Seven out of the ten sensors showed peaks in standard deviations starting at angles of attack 12° and 13°, so in stall. Six of these sensors showed a drop at 20°, which was discovered to be caused by the sensors being stuck in a curled up position. So it can be concluded that stall can be measured using the standard deviation of the output of the strain gauge sensors if the sensor does not get stuck in one position.

The standard deviation of the sensors do not show correlation with the DC values of the sensors. However, the three sensors that do not show an increase in standard deviation in stall, the sensors with a rectangular base and a strain gauge length of 5 mm, 10 mm and 15 mm, belong to the group with differences between the four and two point resistance measurements ranging up to multiple hundreds of kilo ohms. Their could be a relation between this or it could be caused by the fact that these are sensors with a rectangular base and a strain gauge length of 15 mm and smaller.

Four out of the five sensors with a rectangular base show deviations up to $160\ \Omega$ where only two out of the five sensors with a gap in the base reach the deviations of $160\ \Omega$. This could indicate that the sensors with a rectangular base have more deviations. But three of those four sensors with a rectangular base are the sensors that did not have peaks in deviation in stall. So that would indicate that the sensors with a gap in the base are better at measuring stall.

To investigate this further, the same follow-up researches as recommended in section 6.3.2 could be done. So changing the method for attaching contacts, using a four points measurement, testing on multiple sensors with the same dimensions and measuring at more angles of attack. A good addition would be to use a lock-in amplifier to minimize the noise and get a better overview on the frequencies which the sensor works on.

Another interesting research would be to measure the reaction time of the sensor. This could be done by syncing the time of the wind tunnel computer and the myDAQ and measuring the standard deviation, of a certain time step size, and the angle of attack over time and analysing the correlations between the standard deviation and angle of attack.

The magnitude of the standard deviation differs per sensors, some stay below $40\ \Omega$ and others reach up to $160\ \Omega$. The magnitude of this standard deviation could be influenced by the resistor values of the Wheatstone bridge, since higher resistances are measured with a lower accuracy than the lower resistances, see section 4.1.3. However this does not seem to be the main reason for the difference in magnitude of the standard deviation. The sensors with a standard deviation up to $160\ \Omega$ have means from $3\ \text{k}\Omega$ to $8.8\ \text{k}\Omega$ while the sensors with a standard deviation below $40\ \Omega$ have means from $1.1\ \text{k}\Omega$ to $7\ \text{k}\Omega$. The Wheatstone bridge could still have an effect on the standard deviation and this might be interesting for a follow-up research. This could be investigated by using different resistor values in the Wheatstone bridge.

6.4 Conclusion

The conclusion and limitations of the analysis of the mechanical properties of the sensor are explained. The limitations of the method of testing are also explained. From the results of DC analysis can be derived that there are uncertainty's in the results and further analysis should be done. The results of the AC analysis show measurable behaviour in seven of the ten sensors and with further optimization these results can be improved. There is no proof that the sensor design with a gap works better than the rectangular sensor as was concluded from the theoretical analysis.

7 Conclusion

In this report, the theoretical analysis, design, fabrication, testing and evaluation of a strain gauge based flow sensor is done. Twenty-one sensor without a strain gauge with heights varying from 0.1 mm to 0.7 mm and lengths varying from 36.4 mm to 127.5 mm are designed and tested. And ten sensors with a strain gauge, a height of 0.3 mm, a length of 70 mm, strain gauge lengths from 5 to 25 mm and two different structures are designed and tested.

The main research question in this report is:

“How can the presence of flow reversal at the suction side of an airfoil be measured using a 3D-printed flow sensor?”

This question is supported by three sub questions which were answered in this research.

The first question is: "How do mechanical properties of the materials and the structure influence the performance of the strain gauge theoretically?" In chapter 2, it was concluded that the difference in Young's modules between the materials of the sensor, Ninjaflex and PI-ETPU, need to be taken into account in designing the sensor. Furthermore it was concluded that a neutral axis as far away from the strain gauge and a small second moment of area are preferred for optimal results and two design cross sections were introduced. With further analysis the working of the strain gauge could be understood better to design a more optimal sensor.

The second question is: "How is the Cauchy ratio related to the aeroelastic behaviour of the sensor?" In section 6.3.1 it was concluded that sensors with the same Cauchy ratios and different dimensions show different behaviour. The bigger and thus heavier sensors show less movement and this could be caused by gravity, this can be tested in the future by comparing tests where the sensor is placed on the top and on the bottom of the airfoil. For the sensors with a Cauchy ratio above 1158.3 this effect is less significant, they all show the behaviour of bending. A flow sensor with a Cauchy ratio above this value is thus best as it shows the most movement and thus has the most significant output. A better analysis of the relation between the Cauchy ratio and the aeroelastic behaviour could be done by testing more sensors with different dimensions and the same Cauchy ratio. This conclusion is limited by the Cauchy ratio's and the dimension of the sensors that were tested.

The last question is: "How can the aeroelastic behaviour of the sensor be determined using the output of the strain gauge?" In section 6.3.2 it was concluded that the contact resistance influences the DC output of the sensor significantly. A four point measurement might minimize this influence and different contacts can decrease the contact resistance. In section 6.3.3 it was concluded that stall can be measured using the standard deviation of the output of the strain gauge sensors if the sensor does not get stuck in one position. With further analysis using four point measurement, testing multiple sensors with the same dimensions and measuring at more angles of attack the sensor can be further optimized.

With these conclusions the research question can be answered. Flow reversal can be measured at the suction side of an airfoil using the standard deviation of a 3D-printed piezoresistive strain gauge based flow sensor. A neutral axis as far away from the strain gauge and a small second moment of area theoretically improve the performance of the strain gauge. Sensors with a Cauchy ratio above 1158.3 within the tested dimension of a height between 0.1 mm and 0.7 mm and length between 36.4 mm and 127.5 mm are expected to have the most significant outputs.

Because of this research flow sensors for quickly changing flows can be made and optimized. In particular, the Robotics and Mechatronics work group of the University of Twente can use this flow sensor to study the airflow around the wings of the Robird better.

A Formulas

Neutral axis of the structure in figure 2.3:

$$\begin{aligned}\bar{y} &= \frac{A_{\text{Ninjaflex}} \cdot \bar{y}_{\text{Ninjaflex}} + n A_{\text{PI-ETPU}} \cdot \bar{y}_{\text{PI-ETPU}}}{A_{\text{Ninjaflex}} + n A_{\text{PI-ETPU}}} \\ &= \frac{b_1 h_1 \cdot \frac{1}{2} h_1 + \frac{3}{2} \cdot 2 b_2 h_2 \cdot (\frac{1}{2} h_2 + h_1)}{b_1 h_1 + \frac{3}{2} \cdot 2 b_2 h_2} \\ &= \frac{b_1 h_1^2 + 6 b_2 h_1 h_2 + 3 b_2 h_2^2}{2 b_1 h_1 + 6 b_2 h_2}\end{aligned}\quad (\text{A.1})$$

Neutral axis of the structure in figure 2.4:

$$\begin{aligned}\bar{y}_{\text{gap}} &= \frac{A_{\text{Ninjaflex}, 1} \cdot \bar{y}_{\text{Ninjaflex}, 1} + A_{\text{Ninjaflex}, 2} \cdot \bar{y}_{\text{Ninjaflex}, 2} + n A_{\text{PI-ETPU}} \cdot \bar{y}_{\text{PI-ETPU}}}{A_{\text{Ninjaflex}, 1} + A_{\text{Ninjaflex}, 2} + n A_{\text{PI-ETPU}}} \\ &= \frac{b_1 (h_1 - h_3) \cdot \frac{1}{2} (h_1 - h_3) + 2 b_2 h_3 \cdot (h_1 - \frac{1}{2} h_3) + \frac{3}{2} \cdot 2 b_2 h_2 \cdot (\frac{1}{2} h_2 + h_1)}{b_1 (h_1 - h_3) + 2 b_2 h_3 + \frac{3}{2} \cdot 2 b_2 h_2} \\ &= \frac{b_1 (h_1 - h_3)^2 + b_2 (3 h_2 (2 h_1 + h_2) + 4 h_1 h_3 - 2 h_3^2)}{2 b_1 (h_1 - h_3) + 2 b_2 (3 h_2 + 2 h_3)}\end{aligned}\quad (\text{A.2})$$

For the structure in figure 2.3 the second moment of area is:

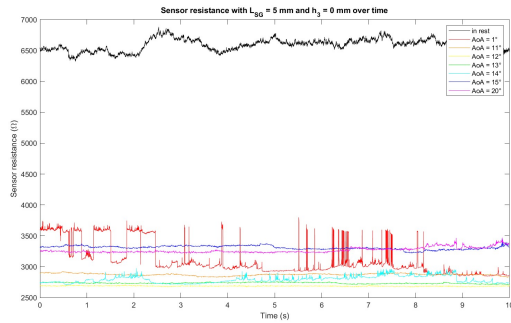
$$\begin{aligned}I_x &= \int_{-\frac{b_1}{2}}^{\frac{b_1}{2}} \int_{-\bar{y}}^{h_1 - \bar{y}} y^2 dy dx + n \cdot \int_{\frac{b_1}{2} - b_2}^{\frac{b_1}{2}} \int_{h_1 - \bar{y}}^{h_1 + h_2 - \bar{y}} y^2 dy dx + n \cdot \int_{-\frac{b_1}{2}}^{-\frac{b_1}{2} + b_2} \int_{h_1 - \bar{y}}^{h_1 + h_2 - \bar{y}} y^2 dy dx \\ I_x &= \frac{1}{3} b_1 ((h_1 - \bar{y})^3 + \bar{y}^3) + n \left(\frac{2}{3} b_2 ((h_1 + h_2 - \bar{y})^3 - (h_1 - \bar{y})^3) \right)\end{aligned}\quad (\text{A.3})$$

For the structure in figure 2.4 the second moment of area is:

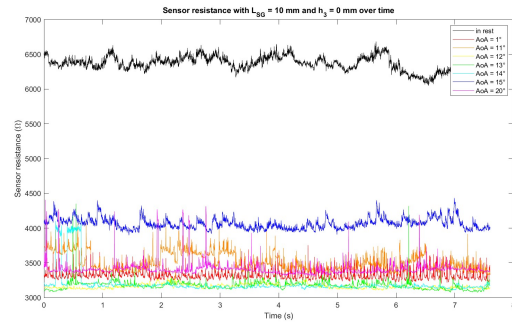
$$\begin{aligned}I_{x, \text{gap}} &= \frac{1}{3} b_1 ((h_1 - \bar{y}_{\text{gap}})^3 + \bar{y}_{\text{gap}}^3) + n \left(\frac{2}{3} b_2 ((h_1 + h_2 - \bar{y}_{\text{gap}})^3 - (h_1 - \bar{y}_{\text{gap}})^3) \right) - \int_{-\frac{b_1}{2} + b_2}^{\frac{b_1}{2} - b_2} \int_{h_1 - h_3 - \bar{y}}^{h_1 - \bar{y}} y^2 dy dx \\ I_{x, \text{gap}} &= \frac{1}{3} b_1 ((h_1 - \bar{y}_{\text{gap}})^3 + \bar{y}_{\text{gap}}^3) - \frac{1}{3} (b_1 - 2 b_2) ((h_1 - \bar{y}_{\text{gap}})^3 - (h_1 - h_3 - \bar{y}_{\text{gap}})^3) \\ &\quad + n \left(\frac{2}{3} b_2 ((h_1 + h_2 - \bar{y}_{\text{gap}})^3 - (h_1 - \bar{y}_{\text{gap}})^3) \right)\end{aligned}\quad (\text{A.4})$$

B Results

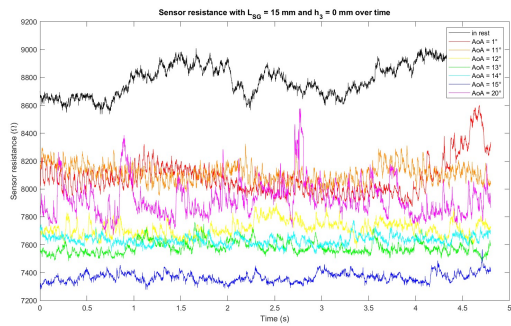
B.1 Resistance change of sensors with strain gauges over time



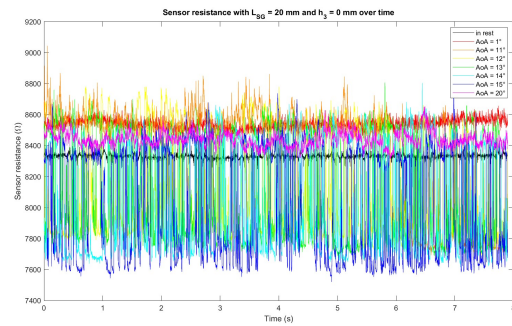
(a) Sensor with a strain gauge length of 5 mm



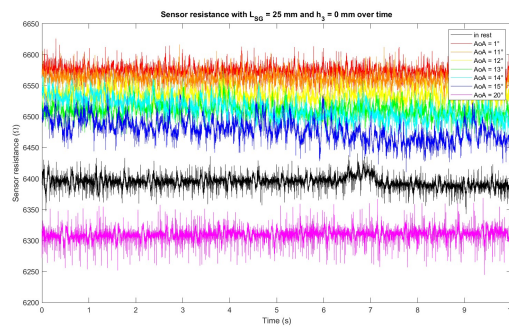
(b) Sensor with a strain gauge length of 10 mm



(c) Sensor with a strain gauge length of 15 mm

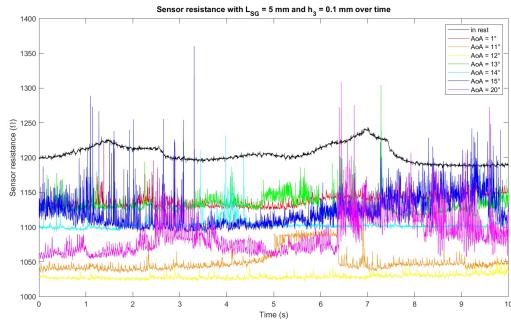


(d) Sensor with a strain gauge length of 20 mm

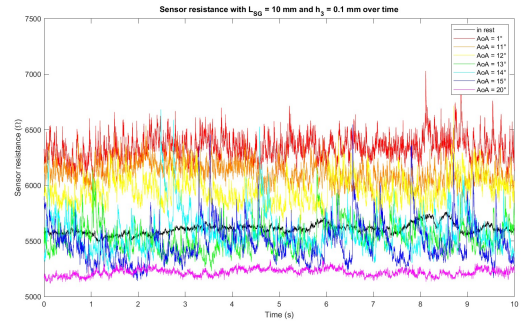


(e) Sensor with a strain gauge length of 25 mm

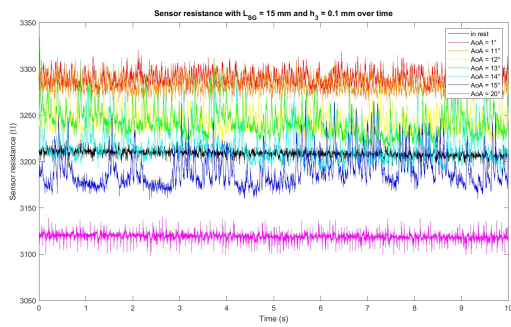
Figure B.1: Time spectrum of the resistor change of the rectangular sensors



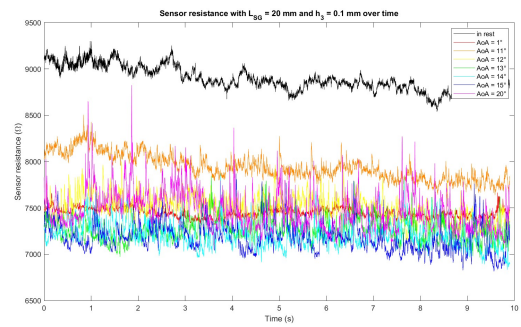
(a) Sensor with a strain gauge length of 5 mm



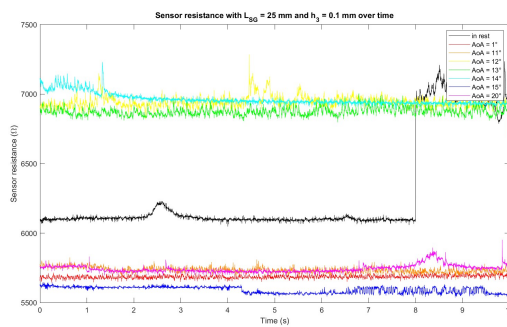
(b) Sensor with a strain gauge length of 10 mm



(c) Sensor with a strain gauge length of 15 mm



(d) Sensor with a strain gauge length of 20 mm



(e) Sensor with a strain gauge length of 25 mm

Figure B.2: Time spectrum of the resistor change of the sensors with a gap

B.2 Resistance means of sensors with strain gauges

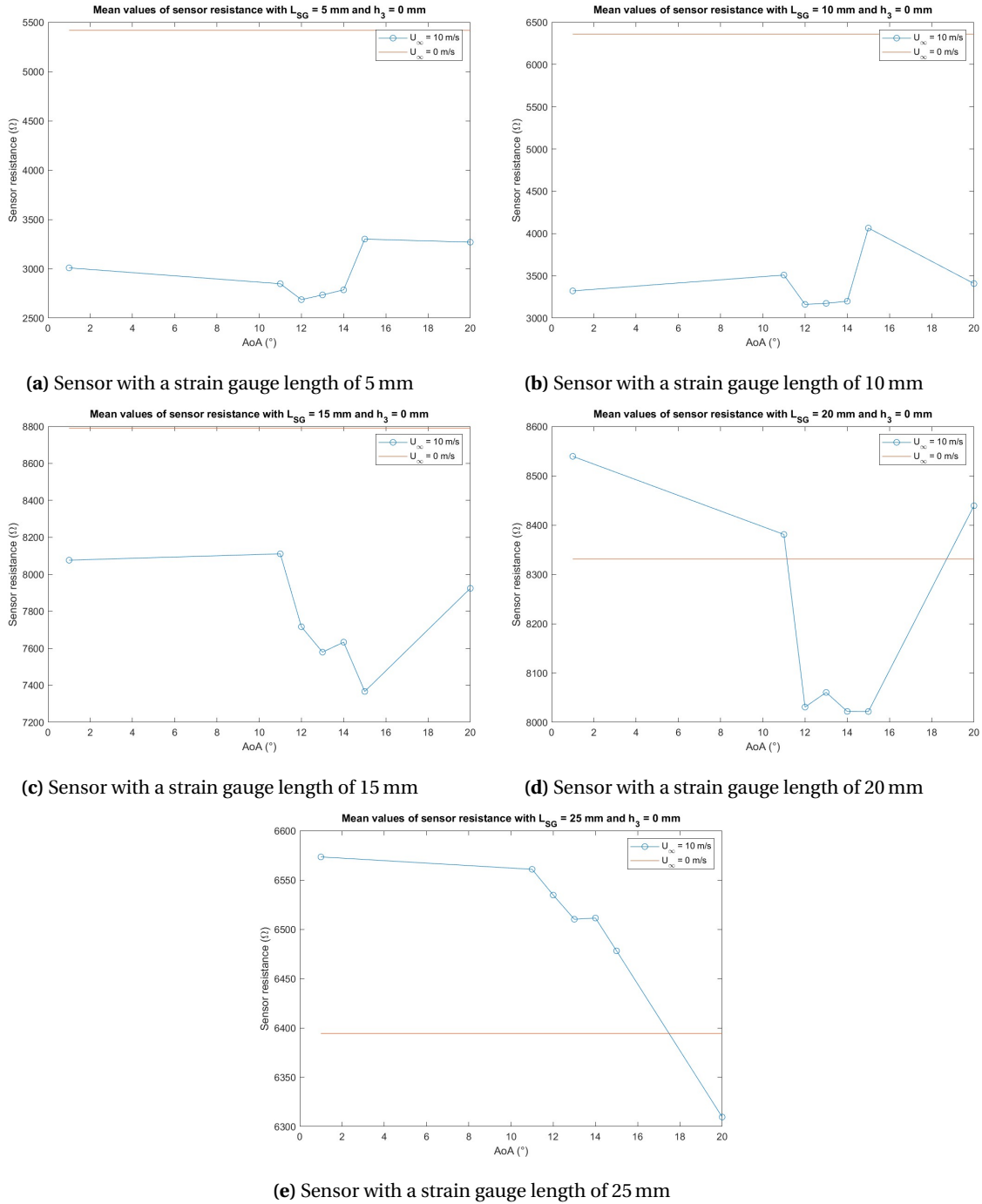
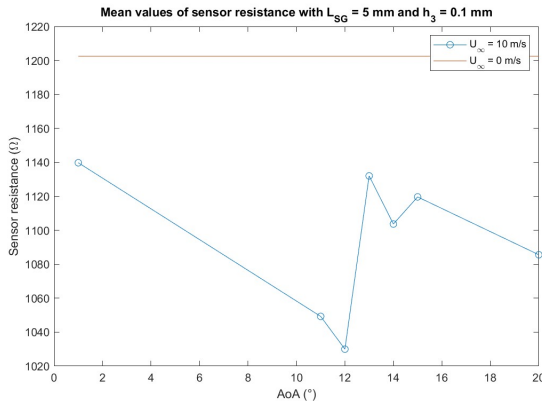
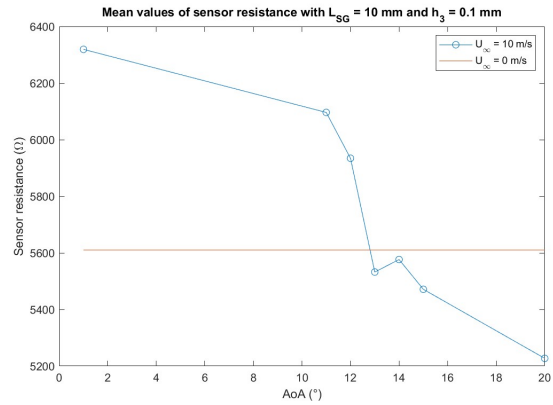


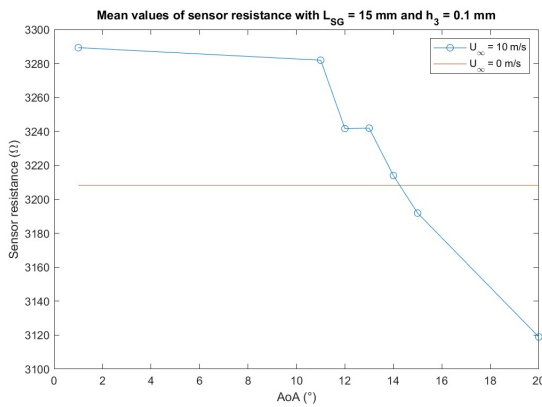
Figure B.3: Means of the resistor change of the rectangular sensors



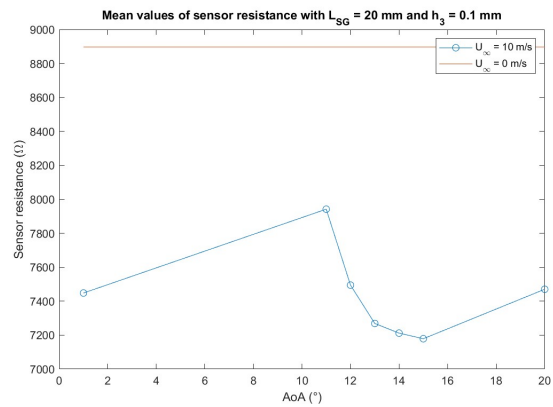
(a) Sensor with a strain gauge length of 5 mm



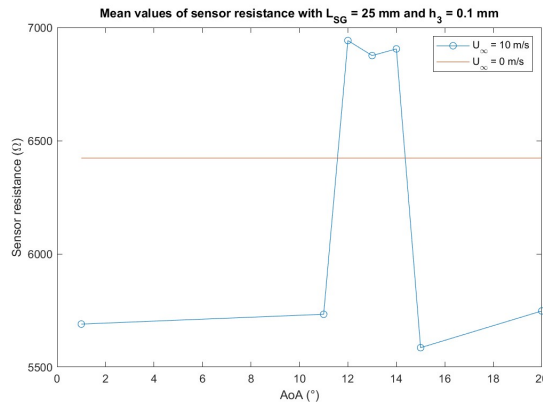
(b) Sensor with a strain gauge length of 10 mm



(c) Sensor with a strain gauge length of 15 mm



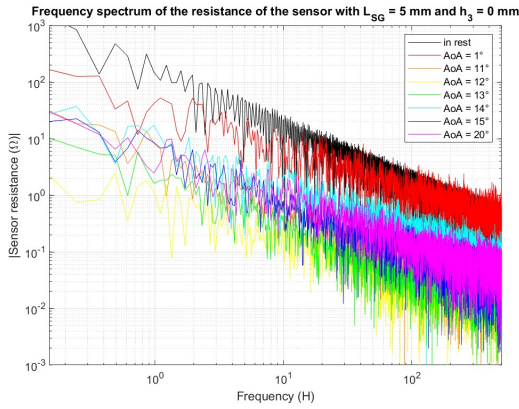
(d) Sensor with a strain gauge length of 20 mm



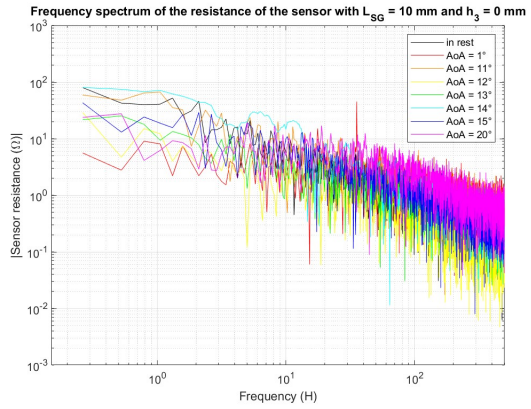
(e) Sensor with a strain gauge length of 25 mm

Figure B.4: Means of the resistor change of the sensors with a gap

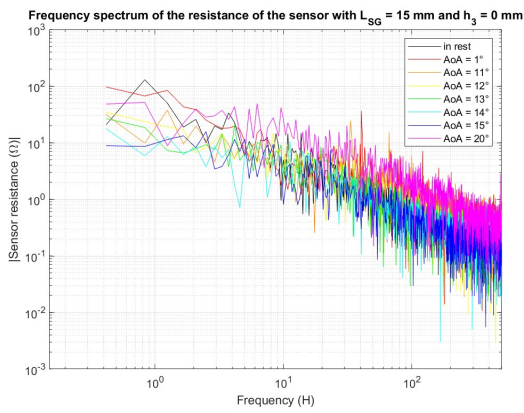
B.3 Frequency spectrum of sensors with strain gauges



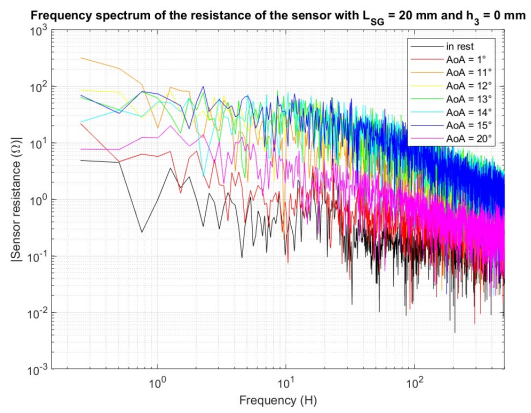
(a) Sensor with a strain gauge length of 5 mm



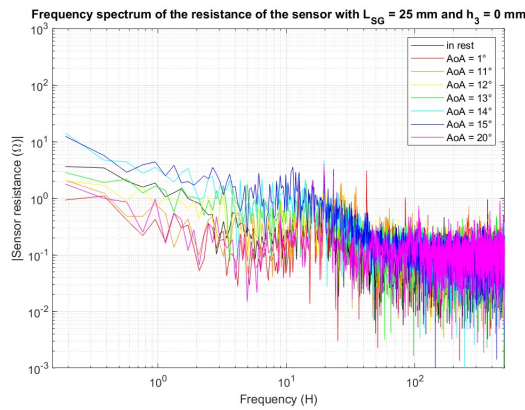
(b) Sensor with a strain gauge length of 10 mm



(c) Sensor with a strain gauge length of 15 mm



(d) Sensor with a strain gauge length of 20 mm



(e) Sensor with a strain gauge length of 25 mm

Figure B.5: Frequency spectrum of the resistor change of the rectangular sensors

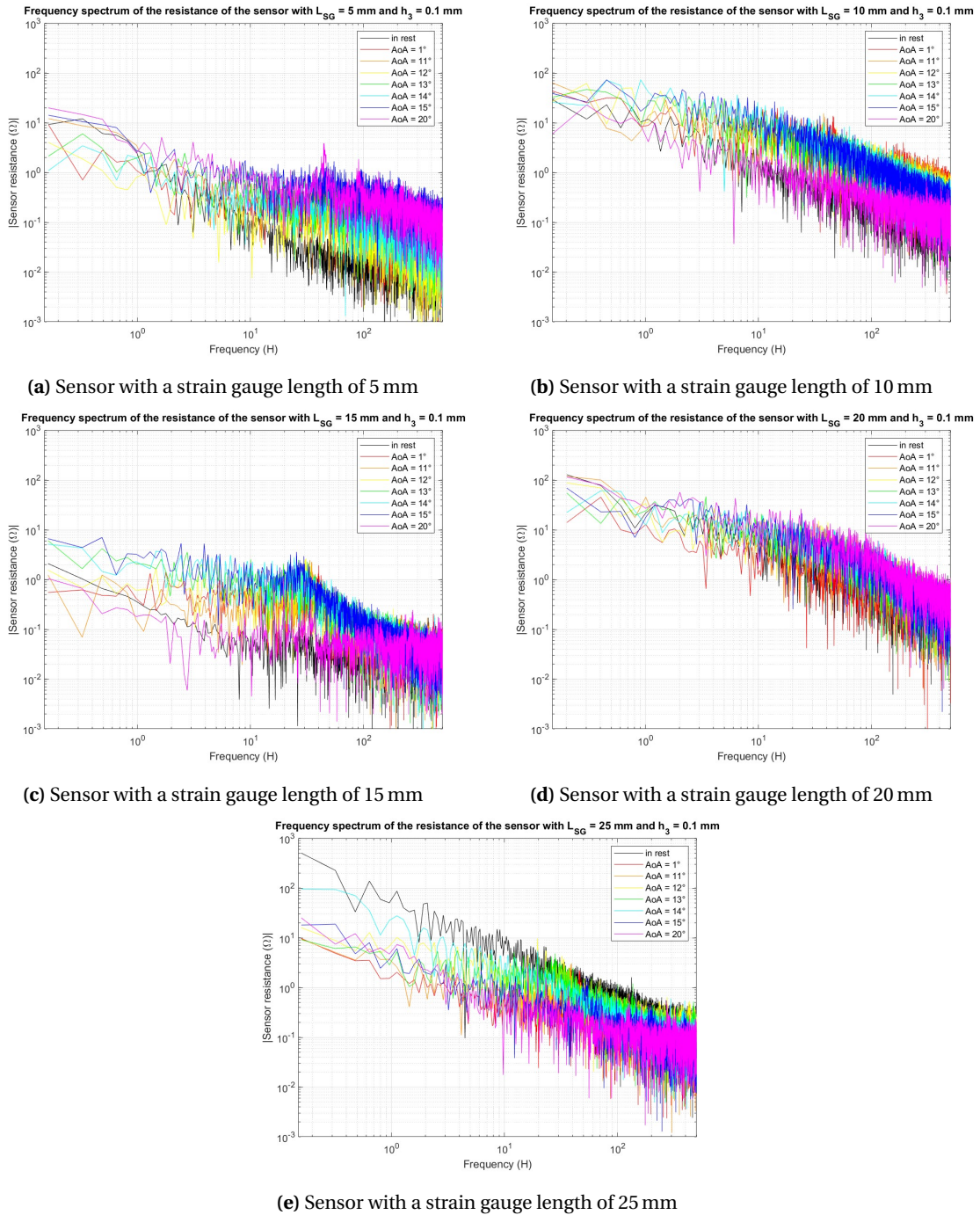


Figure B.6: Frequency spectrum of the resistor change of the sensors with a gap

B.4 Resistance standard deviation of sensors with strain gauges

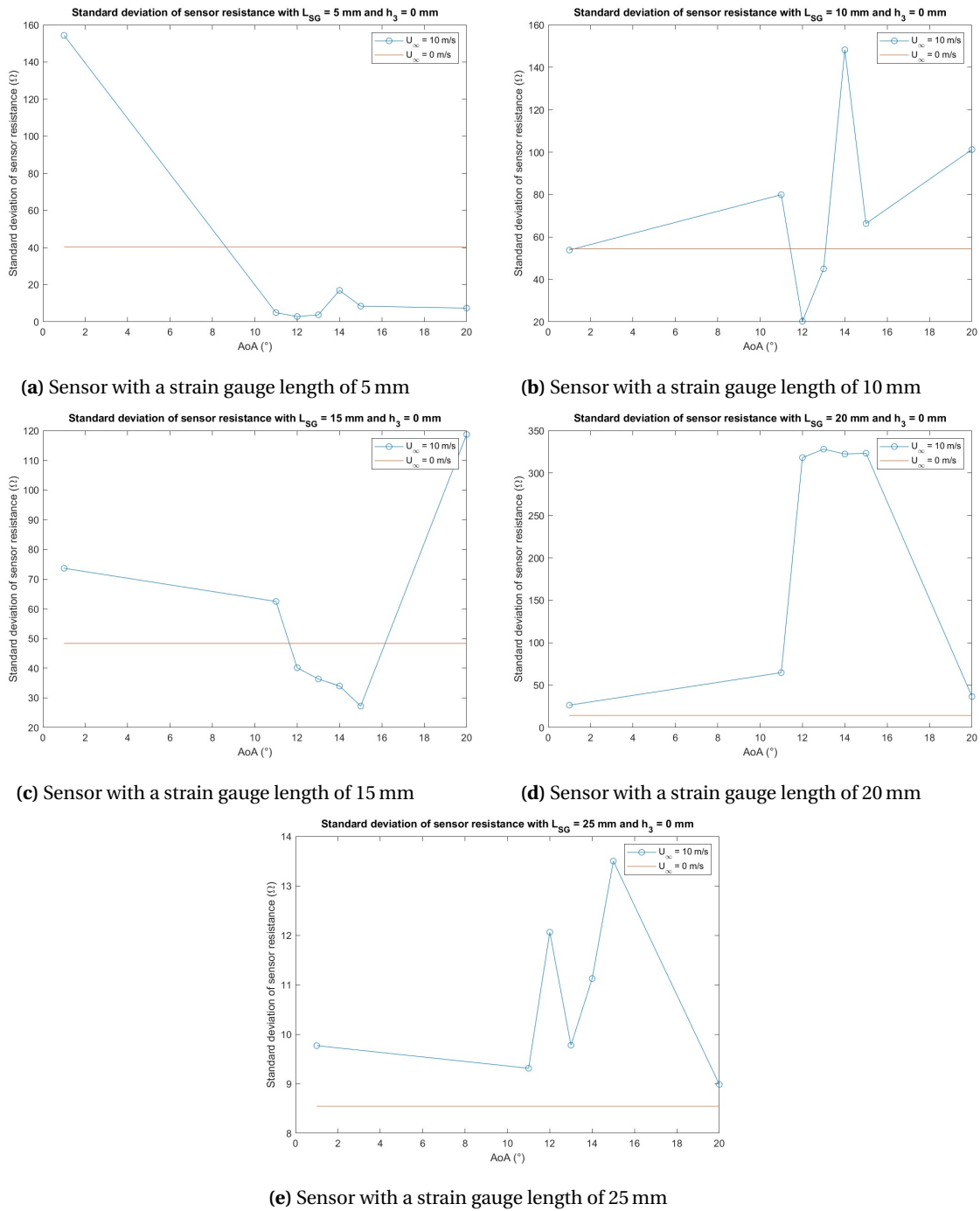


Figure B.7: Standard deviation of the resistor change of the rectangular sensors after a 1 Hz high pass filter

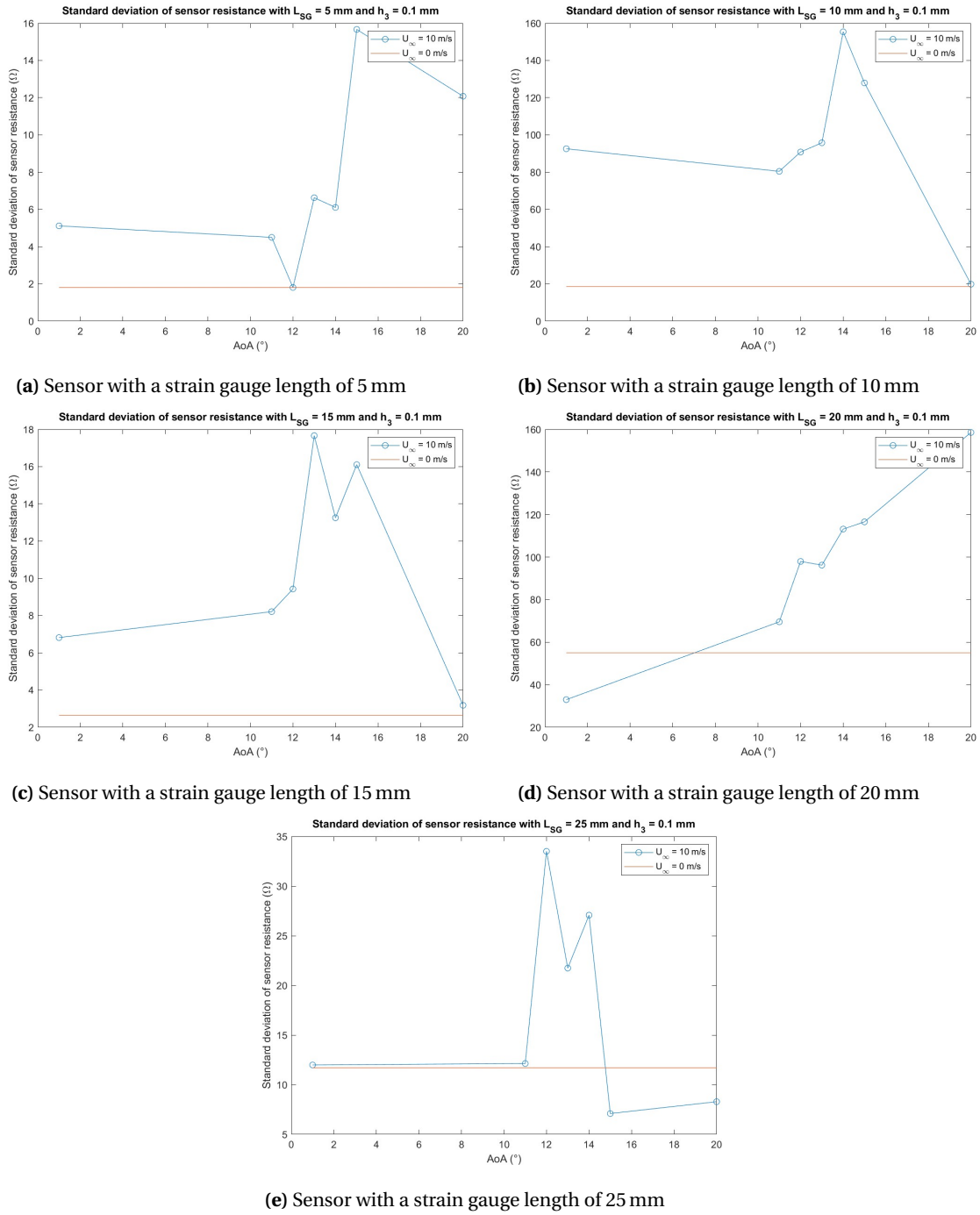


Figure B.8: Standard deviation of the resistor change of the sensors with a gap after a 1 Hz high pass filter

Nomenclature

List of Symbols

α	angle of attack (°)
\bar{y}	height neutral axis over x (m)
μ	Poisson's ratio (-)
\mathcal{S}	slenderness ratio (-)
ρ	resistivity (Ωm)
ρ_f	density of fluid (kg/m^3)
ρ_s	density of solid (kg/m^3)
σ	standard deviation (same unit as what it is the standard deviation of)
A	Axial Force (N)
A	cross-section area (m^2)
b	width (m)
c	chord length (m)
c_D	Drag coefficient (-)
c_L	Lift coefficient (-)
Ca	Cauchy number (-)
D	Drag (N)
E	Young's modulus (N/m^2)
F_s	sampling frequency (Hz)
h	height (m)
I_x	second moment of area in the x direction (m^4)
K	Bulk modulus of elasticity (N/m^2)
L	Lift (N)
l	length (m)
N	Normal Force (N)
n	ratio between Young's moduli (-)
q	dynamic pressure (Pa)
R	resistance (Ω)
r_a	radius of gyration (m)

Re	Reynolds number (-)
S	wing area (m^2)
t	time (s)
U	flow velocity (ms^{-1})
U_{∞}	free stream velocity (ms^{-1})
V_{in}	input voltage (V)
V_{out}	output voltage (V)

List of Abbreviations

AOA	angle of attack
FDM	fused deposition modeling
FFT	fast fourier transform
RaM	Robotics and Mechatronics
std	standard deviation
TPU	thermoplastic polyurethane

Bibliography

- [1] F. Califano, R. Rashad, A. Dijkshoorn, L. G. Koerkamp, R. Sneep, A. Brugnoli, and S. Stramigioli, "Decoding and realising flapping flight with port-hamiltonian system theory," *Annual Reviews in Control*, vol. 51, pp. 37–46, 2021.
- [2] Farnell, "Air flow sensors." <https://nl.farnell.com/c/sensors-transducers/sensors/flow-sensors/air-flow-sensors>. Accessed: June 24, 2022.
- [3] R. van den Berg, "Qualitative flow sensing with 3d-printed sensors for application in a robotic bird," June 2021.
- [4] P. Bot, R. Alas, D. Voisin, A. Soulier, C. Braud, P. Marcillat, B. Pezeril, and F. d'Arco, "Characterization of a flow separation sensor on a hydrofoil: The hydro e-telltale," March 2021.
- [5] W. Shyy, H. Aono, C.-K. Kang, and H. Liu, *An Introduction to Flapping Wing Aerodynamics*. Cambridge University Press, 2013.
- [6] G. A. Folkertsma, W. Straatman, N. Nijenhuis, C. H. Venner, and S. Stramigioli, "Robird: A robotic bird of prey," *IEEE Robotics & Automation Magazine*, vol. 24, no. 3, pp. 22–29, 2017.
- [7] S. J. Ling, J. Sanny, W. Moebis, D. Janzen, and et al., *Introduction to Electricity, Magnetism, and Circuits*. University of Saskatchewan, Nov 2018.
- [8] Avnet, "Piezoresistive pressure sensors." <https://www.avnet.com/wps/portal/abacus/solutions/technologies/sensors/pressure-sensors/core-technologies/piezoresistive-strain-gauge/>. Accessed: July 21, 2022.
- [9] G. Saggio, F. Riillo, L. Sbernini, and L. R. Quitadamo, "Resistive flex sensors: a survey," *Smart Materials and Structures*, vol. 25, p. 013001, dec 2015.
- [10] Build Right, "Beams - neutral axis." https://www.dlsweb.rmit.edu.au/Toolbox/buildright/content/bcgbc4010a/04_struct_members/01_beams/page_003.htm. Accessed: July 13, 2022.
- [11] L. Carolo, "Fused deposition modeling: Fdm 3d printing simply explained." <https://all3dp.com/2/fused-deposition-modeling-fdm-3d-printing-simply-explained/>, June 2022. Accessed: July 14, 2022.
- [12] Ninjatek, "Ninjaxflex 3d printer filament (85a)." <https://ninjatek.com/shop/ninjaxflex/>. Accessed: July 4, 2022.
- [13] Palmiga Innovation, "Material info for pi-etpu 95-250 carbon black the conductive and flexible 3d printing filament." <http://rubber3dprinting.com/pi-etpu-95-250-carbon-black/>. Accessed: July 14, 2022.
- [14] A. Dijkshoorn, M. Schouten, S. Stramigioli, and G. Krijnen, "Modelling of anisotropic electrical conduction in layered structures 3d-printed with fused deposition modelling," *Sensors*, vol. 21, no. 11, 2021.
- [15] D. Kosmas, "Model-based hysteresis compensation and control with 3d printed lousy sensors." <http://essay.utwente.nl/84814/>, October 2020.

- [16] TWI, “What is annealing? a complete process guide.” <https://www.twi-global.com/technical-knowledge/faqs/what-is-annealing>. Accessed: July 23, 2022.
- [17] M. Schouten, “Towards additively manufactured complex robotic systems.” <http://essay.utwente.nl/74355/>, December 2017.
- [18] R. Hibbeler, *Mechanics of Materials, 8th Edition*. Pearson Prentice Hall, 2010.
- [19] Mech Content, “Neutral axis: Definition, diagram, formula, for different shapes [with pdf].” <https://mechcontent.com/neutral-axis/>, February 2022. Accessed: May 17, 2022.
- [20] R. Pierce, “Moments of area.” <http://www.mathsisfun.com/geometry/area-moments.html>, October 2021.
- [21] A. C. Ugural and S. K. Fenster, “Chapter 5.9 - composite beams,” in *Advanced mechanics of materials and applied elasticity*, August 2019.
- [22] D. Rosato and D. Rosato, “PRODUCT DESIGN,” in *Plastics Engineered Product Design*, pp. 198–343, Elsevier, 2003.
- [23] R. Hibbeler, *Mechanics of Materials, 8th Edition*. Pearson Prentice Hall, 2010.
- [24] L. Skinner, “Chapter 4 - snubbing theory and calculations,” in *Hydraulic Rig Technology and Operations* (L. Skinner, ed.), Gulf Drilling Guides, pp. 189–275, Gulf Professional Publishing, 2019.
- [25] J. D. Anderson, *Fundamentals of Aerodynamics*. McGraw-Hill, 6th ed., 2016.
- [26] J. B. Barlow, W. H. Rae, and A. Pope, *Low-Speed Wind Tunnel Testing, 3rd Edition*. 1999.
- [27] J. R. Wright and J. E. Cooper, “Introduction to aircraft aeroelasticity and loads,” pp. 1–6, 2014.
- [28] Engineering ToolBox, “Cauchy number.” https://www.engineeringtoolbox.com/cauchy-number-d_580.html, 2004. Accessed: June 29, 2022.
- [29] extrudesign.com, “What is bulk modulus? | bulk modulus vs young’s modulus vs rigidity modulus.” <https://extrudesign.com/bulk-modulus-vs-youngs-modulus-vs-shear-modulus/>, April 2018. Accessed: July 24, 2022.
- [30] G. GRIMVALL, “Chapter 3 - elasticity. basic relations,” in *Thermophysical Properties of Materials* (G. GRIMVALL, ed.), pp. 27–45, Amsterdam: Elsevier Science B.V., 1999.
- [31] R. Elleuch, K. Elleuch, B. Salah, and H. Zahouani, “Tribological behavior of thermoplastic polyurethane elastomers,” *Materials Design*, vol. 28, no. 3, pp. 824–830, 2007.
- [32] H. Qi and M. Boyce, “Stress–strain behavior of thermoplastic polyurethanes,” *Mechanics of Materials*, vol. 37, no. 8, pp. 817–839, 2005.
- [33] E. de Langre, “Effects of wind on plants,” *Annual Review of Fluid Mechanics*, vol. 40, pp. 141–168, jan 2008.
- [34] “Rotary 3d printer + cnc mill | diabase engineering | united states.” <https://www.diabasemachines.com/hseries>. Accessed: June 5, 2022.

- [35] 3DHerndon, “Diabase h4 pro.” <https://3dherndon.com/diabase-engineering-5-axis-h-series-hybrid-3d-printer-and-cnc-mill.html>. Accessed: June 23, 2022.
- [36] “Ultimaker cura.” <https://ultimaker.com/nl/software/ultimaker-cura>. Accessed: June 5, 2022.
- [37] Aerolab, “Educational wind tunnel (ewt).” <https://www.aerolab.com/aerolab-products/educational-wind-tunnel-ewt/>. Accessed: June 21, 2022.
- [38] Casio computer Co., “Casio exilim ex-f1.” http://arch.casio-intl.com/asia-mea/en/dc/ex_f1/. Accessed: July 1, 2022.
- [39] S. Vouyiouka and C. Papaspyrides, “4.34 - mechanistic aspects of solid-state polycondensation,” in *Polymer Science: A Comprehensive Reference* (K. Matyjaszewski and M. Möller, eds.), pp. 857–874, Amsterdam: Elsevier, 2012.
- [40] Electronics Tutorials, “Wheatstone bridge circuit and theory of operation.” <https://www.electronics-tutorials.ws/blog/wheatstone-bridge.html>, April 2021. Accessed: June 29, 2022.
- [41] National Instruments, “mydaq student data acquisition device.” <https://www.ni.com/nl-nl/shop/hardware/products/mydaq-student-data-acquisition-device.html>. Accessed: July 1, 2022.
- [42] Keysight technologies, “34401a digital multimeter.” <https://www.keysight.com/us/en/assets/7018-06774/data-sheets/5968-0162.pdf>. Accessed: July 4, 2022.
- [43] National Instruments, “Ni mydaq specifications.” <https://www.ni.com/docs/en-US/bundle/mydaq-specs/page/specs.html>, November 2021. Accessed: July 13, 2022.